FREQUENCY-CONVERSION OPTICS FOR 213-NM OPTICAL LITHOGRAPHY LIGHT SOURCE

by

Edita Tejnil

Memorandum No. UCB/ERL M94/27

14 April 1994

FREQUENCY-CONVERSION OPTICS FOR 213-NM OPTICAL LITHOGRAPHY LIGHT SOURCE

by

Edita Tejnil

Memorandum No. UCB/ERL M94/27

14 April 1994

ELECTRONICS RESEARCH LABORATORY

College of Engineering
University of California, Berkeley
94720

FREQUENCY-CONVERSION OPTICS FOR 213-NM OPTICAL LITHOGRAPHY LIGHT SOURCE

by

Edita Tejnil

Memorandum No. UCB/ERL M94/27

14 April 1994

ELECTRONICS RESEARCH LABORATORY

College of Engineering
University of California, Berkeley
94720

Frequency-Conversion Optics for 213-nm Optical Lithography Light Source

Edita Tejnil

M. S. Project
Spring 1994

Professor W. G. Oldham
Department of Electrical Engineering and Computer Sciences
University of California at Berkeley

Abstract

Harmonic generation for high-power, deep-UV light source to be used in optical lithography is described. Quintupling of the Nd:YAG laser frequency to 213 nm is considered. Nonlinear crystals and other optical components used in the system are described. The design of the three-stage, colinear harmonic generator is considered in detail, with emphasis on crystal heating, conversion efficiency, and nonlinear material properties. The design process presented here is applicable to multi-stage optical frequency up-conversion in general.

Table of Contents

1.0 Introduction

The size of integrated circuit devices is ultimately limited by the wavelength of light source used for patterning the circuit features. The shortest wavelengths available for optical lithography are in the deep-ultraviolet region of the spectrum. Presently, the best-developed light sources in the deep-UV are the mercury lamp I-line at wavelength of 365 nm and the KrF excimer laser at 248 nm. In recent years, interest in lithography sources with shorter wavelengths has been focused on the ArF excimer laser at 193 nm and the quintupled Nd:YAG laser at 213 nm. The 213 nm light source is the topic of this report.

The first generation 213-nm source for lithography was demonstrated by Partlo [1] and is currently in use at UC Berkeley. The 213-nm light source consists of a Nd:YAG laser followed by a nonlinear frequency quintupler. The Nd:YAG laser produces 4.1 Watts of average power at the 1064-nm wavelength. This flashlamp-pumped laser, which operates at 10-Hz repetition rate, produces short, high-intensity pulses by Q-switching and is injection-seeded to produce stable optical frequency, single-mode output with narrow spectral linewidth. The harmonic generator has three stages of nonlinear crystals capable of optical sum-frequency generation. The first stage is a KD*P crystal frequency doubler utilizing type II frequency mixing. The second stage, also a type II frequency mixing KD*P crystal, produces the third harmonic from its first- and second-harmonic inputs. The third stage, which adds the second and the third harmonics to produce the fifth harmonic, consists of a BBO crystal oriented for type I frequency mixing. This system produces at most 0.25 Watts of 213-nm radiation and outputs approximately 0.1 Watts under typical operating conditions. Features 0.2 μm in size have been patterned on silicon with this system.

In the spectral region near the 200 nm, optical lithography becomes limited by absorption of most materials available for making refractive optics. Among conventional optical materials, only quartz and synthetic fused silica have sufficient transmission at these wavelengths to be used in lithography imaging systems. In the deep-UV, absorption and material damage rates are smaller at longer wavelengths. Consequently, the life of a 213-nm exposure system is likely to be greater than that of a 193-nm system. Other advantages of the 213-nm source are its narrow spectral linewidth and its frequency stability, which are well within the requirements imposed by the use of refractive optics. On the other hand, it is difficult to obtain stable frequency and narrow bandwidth with the ArF excimer laser. One further advantage of 213-nm system is that it employs mostly solid state materials. Compared to systems that utilize gases (some toxic), it is relatively safe and easy to maintain.

The problems with the 213-nm source include crystal heating and possible optical damage. The heating of the solid-state materials used in the system is caused by absorption and results from the fact the materials are poor thermal conductors, from which heat is not extracted easily. Optical damage is also an issue because the light source inherently operates at high peak intensities.

This report concerns the design of the fifth harmonic generator for the second generation 213-nm light source. The new design is motivated by the desire for higher repetition rate and higher average output power. A new Nd:YAG system was designed to serve as input to the harmonic genera-

tor [2]. The Nd:YAG laser will operate at 1-kHz repetition rate. Like the laser in the first generation system, it will be Q-switched and injection-seeded. The novelty of this laser lies in its pumping by an array of semiconductor laser diodes and its high repetition rate. The laser pulses will be compressed in time to increase the peak intensity to levels sufficient for efficient harmonic conversion. This will be accomplished with stimulated Brillouin scattering before the light enters the harmonic generator. Some of the harmonic generator issues were discussed previously [3]. In this report, the analysis is extended and the final design of the harmonic generation optics for the second generation 213-nm light source is presented. The overview of nonlinear optics issues is given in section 2. Section 3 describes material issues and configuration of the three-stage harmonic generator. Thermal management, important at high average power levels, is the topic of section 4. The issues concerning harmonic conversion efficiency are discussed in section 5. Finally some experimental results are presented in section 6.

2.0 Nonlinear Optics Background

Nonlinear optics is frequently used to convert light of one frequency to other frequencies in order to produce light in those spectral regions where conventional light sources are unavailable. The interactions of light with media make these processes possible. The response of a medium to an optical beam is given by the polarization P,

$$P = \varepsilon_0 (\chi^{(1)} E + \chi^{(2)} E^2 + \chi^{(3)} E^3 + \ldots), \tag{1}$$

where $\chi^{(n)}$ is the n^{th}-order material susceptibility. The first term corresponds to linear optical properties including refraction, absorption or gain, and dispersion. The remaining terms account for the nonlinear response of the medium. For example, the second term, proportional to the square of the electric field, is responsible for sum- and difference-frequency generation. The third term involves the intensity-dependent refractive index of the medium and accounts for such processes as two-photon absorption. In general, the nonlinear susceptibility is small and decreases with order. When strong nonlinear material response is desirable, very large electric fields are required.

The 213-nm light is produced from 1064-nm input with an optical frequency quintupler. Frequency multiplication is accomplished in three consecutive doubling and mixing stages rather than by direct quintupling. Generally, the strongest nonlinear effect is the second-order material response while the fifth-order effect is negligible in comparison. As a result, the second-order mixing can be efficient given sufficient input peak power. On the other hand, efficient direct quintupling would require input peak powers leading to breakdown of most media. Due to symmetry considerations, only solid state materials that lack inversion symmetry possess a non-zero second-order nonlinear susceptibility $\chi^{(2)}$. Thus the harmonic generator for the 213-nm light source consists of nonlinear crystals with appropriate symmetry.

This report concerns the design of an efficient three-stage harmonic generator. The efficiency of frequency doubling and sum-frequency generation can be found by solving the coupled wave

equations for the evolution of complex electric fields at the input and output frequencies. Doubling of a monochromatic continuous-wave beam at frequency ω is described by the coupled wave equations for the slowly varying complex field amplitudes E_1 and E_2 of the first and second harmonic waves. The field evolution in the propagation direction is described by:

$$\frac{\partial E_2}{\partial z} + \frac{\alpha_2}{2}E_2 + \frac{\beta_2}{2}|E_2|^2 E_2 = iCE_1^2 e^{i\Delta kz} \tag{2a}$$

$$\frac{\partial E_1}{\partial z} + \frac{\alpha_1}{2}E_1 + \frac{\beta_1}{2}|E_1|^2 E_1 = iCE_1^* E_2 e^{-i\Delta kz}. \tag{2b}$$

Here the amplitudes are normalized so that the intensities are simply $E_1{}^2$ and $E_2{}^2$. The wavevector mismatch is Δk, linear absorption coefficients at frequencies ω and 2ω are α_1 and α_2, and the two-photon absorption coefficients are β_1 and β_2. The coupling constant C is given by

$$C = \frac{5.456 d_{eff}}{\lambda \sqrt{n_1^2 n_2}}, \tag{3}$$

where d_{eff} is the effective nonlinear coefficient for SHG, and n_1 and n_2 are the refractive indices of the first harmonic wave at frequency $\omega = 2\pi/\lambda$ and its second harmonic at frequency 2ω. The effective nonlinear coefficient d_{eff} depends on the components of the second-order nonlinear susceptibility tensor and on the direction of propagation and polarization of the interacting fields. With this normalization of the fields, the units of E, C, z, d_{eff}, α, β, and λ, are $GW^{1/2}/cm$, $GW^{-1/2}$, cm, pm/V, cm^{-1}, cm/GW, and μm, respectively.

Equations describing sum-frequency generation are analogous to those for second harmonic generation. Here the up-conversion of two input frequencies $a\omega$ and $b\omega$ to the output frequency $c\omega = a\omega + b\omega$ is considered. The complex field equations for E_1, E_2, and E_3 are

$$\frac{\partial E_3}{\partial z} + \frac{\alpha_3}{2}E_3 + \frac{\beta_3}{2}|E_3|^2 E_3 = icCE_1 E_2 e^{i\Delta kz} \tag{4a}$$

$$\frac{\partial E_2}{\partial z} + \frac{\alpha_2}{2}E_2 + \frac{\beta_2}{2}|E_2|^2 E_2 = ibCE_1^* E_3 e^{-i\Delta kz} \tag{4b}$$

$$\frac{\partial E_1}{\partial z} + \frac{\alpha_1}{2}E_1 + \frac{\beta_1}{2}|E_1|^2 E_1 = iaCE_2^* E_3 e^{-i\Delta kz}, \tag{4c}$$

where the field amplitudes are again normalized so that the intensities are given by their squared magnitudes. In this case, the coupling constant C is

$$C = \frac{5.456 d_{eff}}{\lambda \sqrt{n_1 n_2 n_3}}, \tag{5}$$

where n_1, n_2, and n_3 are the refractive indices of the nonlinear material at frequencies $a\omega$, $b\omega$, and $c\omega$. The other parameters and their units are described above. The solutions to the coupled wave equations will be discussed in section 5. Presently, it is important to note that the solutions are oscillatory in the direction of propagation.

The extent to which the input energy is converted to energy at the harmonic frequency depends on the strength of the nonlinear coupling and on the phase mismatch of the interacting fields. Harmonic generation can be efficient only when the nonlinear driving term is large. Since strong nonlinear coupling is required for efficient conversion, the nonlinear medium of choice for a given frequency conversion process is one with large effective nonlinear coefficient d_{eff} for that process. Large peak input intensities are also needed for high conversion efficiency. In addition to a large driving term, it is necessary to maintain the interacting beams in phase, which corresponds to keeping the phase mismatch Δk as small as possible. When the beams are not in phase, energy is converted to the harmonic frequency, but before it can build up, it is converted back into the fundamental beams. This happens periodically along the crystal length. The wavevector mismatch of second harmonic generation is $\Delta k = 2k_1 - k_2$, with k_1 and k_2 being the propagation vectors in the nonlinear medium of the input wave and its second harmonic. For collinear beams the perfect phase matching condition $\Delta k = 0$ occurs when

$$n_1 - n_2 = 0 , \tag{6}$$

where n_1 and n_2 are the refractive indices of the nonlinear medium at frequencies ω and 2ω. Similarly, the wavevector mismatch of sum-frequency generation is $\Delta k = k_1 + k_2 - k_3$, with propagation vectors k_1, k_2, and k_3, of waves at frequencies $a\omega$, $b\omega$, and $c\omega = a\omega + b\omega$. For sum-frequency generation the phase matching condition $\Delta k = 0$ is

$$an_1 + bn_2 - cn_3 = 0. \tag{7}$$

The phase-matching requirements would be satisfied in a dispersionless medium but are not met in real materials, which are dispersive. In practice, phase matching is achieved by using the birefringence of the nonlinear crystals. This method takes advantage of the fact that the refractive indices of the TE and TM polarizations depend on the direction of beam propagation with respect to the crystal axes and on temperature. At some fixed crystal temperature, the phase-matching condition can be satisfied by properly orienting the nonlinear crystal with respect to the input beams and by choosing suitably polarized input beams. The phase-matching condition can be achieved in several ways, called type I, type II, and type III, which depend on the polarization of the input beams. In type I phase-matching, the polarization vectors of the two input beams are parallel and the polarization of the output beam is orthogonal to that of the inputs. With type II and type III phase-matching, the input polarization vectors are orthogonal. The way the polarization vectors of the two input beams are oriented with respect to the crystal axes distinguishes between type II and type III phase-matching. The output-beam polarization vector and polarization vector of the input beam at the lower of the two input frequencies are parallel in type II phase-matching, while they are orthogonal in type III phase-matching. These types of phase matching are highly sensitive to the crystal orientation and are thus referred to as critical phase-

matching. The proper crystal orientation can be found in materials that have enough birefringence to compensate for the dispersion between the interacting frequencies. The refractive indices depend not only on crystal orientation but also on temperature. In practice, usually both the crystal orientation and the temperature are controlled simultaneously to obtain stable harmonic conversion.

Ideally, perfect phase-matching can be achieved by tuning the orientation of the crystal and by maintaining its temperature. However, this is not the case in a real frequency up-conversion system due to diffraction effects, imperfect beam quality, crystal inhomogeneities, and nonuniform temperature distribution in the crystal. While crystal inhomogeneities and beam quality are difficult to quantify in efficiency calculations, diffraction effects and temperature nonuniformities can be accounted for by considering the phase matching condition as a function of crystal orientation and temperature. The wavevector mismatch Δk is found by Taylor expansion in the angular and thermal deviations from the phase-matching condition. The expansion is about the crystal temperature T, and about the phase-matching orientation, described by the polar angle θ and azimuthal angle ϕ measured from specified crystal directions,

$$\Delta k = \beta_\theta \Delta\theta + \beta_\phi \Delta\phi + \beta_T \Delta T. \tag{8}$$

This expression is correct to first order in the deviations $\Delta\theta$, $\Delta\phi$, and ΔT. Here the quantities β_θ, β_ϕ, and β_T are the first partial derivatives of the phase mismatch Δk with respect to θ, ϕ, and T, respectively, evaluated at the phase-matching condition. The second term in (8) is present in biaxial crystals but vanishes in uniaxial crystals because of their azimuthal symmetry about the optic axis. Since the phase mismatch is also a function of frequency, Eq. (8) can be extended to account for the finite spectral bandwidth of the interacting beams rather than simply assuming they are monochromatic. However, this effect will be neglected here because the Nd:YAG pump has very high spectral purity. It is also important to note that β_θ and β_ϕ are both zero for certain directions of propagation in birefringent crystals. Provided phase-matching is possible under such conditions, the phase mismatch is determined mainly by the crystal temperature, while the crystal orientation is important only to second order in $\Delta\theta$ and $\Delta\phi$. As a result, this is known as noncritical phase-matching. In some materials, this condition is possible for a specific range of input frequencies and particular crystal temperatures.

The diffraction effects can be modeled by assuming that the finite divergence of the interacting beams results in an effective angular deviation from the phase-matching condition [4]. Similarly in this model, the crystal temperature nonuniformities are taken to be equivalent to temperature deviations. These effects will be discussed further in Sections 4 and 5.

The birefringence associated with phase-matching is important in one other respect. Since the polarizations of the interacting input and output beams are different, the directions of their energy flow differ inside the nonlinear crystal. Given that the input beams are parallel, overlap spatially, and enter the crystal at normal incidence, they will be parallel upon exit from the crystal. However, the spatial overlap of the differently polarized beams will be reduced. This so-called beam walk-off reduces the exchange of energy between the beams inside the nonlinear crystal. In addi-

tion, it is important when several nonlinear stages follow one another. For instance, if the output beam of one stage and the remainder of one of its inputs are to be used as inputs to another nonlinear stage, their spatial overlap is critical to the efficiency of the second stage. There exist certain directions of propagation in birefringent crystals, in which both TE and TM polarizations propagate in the same direction. Under such conditions, the walk-off effect does not occur and higher conversion efficiencies are possible provided the phase-matching condition can be simultaneously satisfied. The propagation direction with no walk-off happens be the same as the direction for noncritical phase-matching.

3.0 Material Issues and Design Overview

Nonlinear material properties are discussed in this section. Crystal geometry and optical components of the three-stage fifth harmonic generator are also described.

3.1 Material issues

The design of the optical frequency quintupler is determined by the properties of the available nonlinear materials. The key properties of interest here include phase-matching properties, nonlinear coupling strength, damage threshold, absorption, and thermal properties. The properties of nonlinear materials most suitable for quintupling the Nd:YAG are the topic of this section. The nonlinear material selection for the 213-nm system was considered previously [3]. Of the numerous material possibilities, few nonlinear materials are suitable for the colinear three-stage system, primarily because only a few are sufficiently transparent over the 1064-213 nm range. In addition, since high conversion efficiency requires high peak intensities, only materials with high damage thresholds can be used. The list of suitable materials is reduced to beta barium borate (BBO), highly deuterated potassium dihydrogen phosphate (KD*P), and lithium borate (LBO).

Tables 1, 2, and 3, summarize the nonlinear optical properties of BBO, KD*P, and LBO, relevant to frequency up-conversion of the Nd:YAG laser. Phase-matching properties, nonlinear coupling strengths, walk-off angles, and tuning properties are given for each up-conversion process. The tables also include the FWHM bandwidths of the angular and thermal tuning curves of crystals of length L, defined as $\Delta\Omega L = 5.56623/\beta_\Omega$ [5], with Ω being θ, ϕ, or T. The tuning bandwidths represent the range of angles or temperatures within which the input beams will significantly contribute to the frequency up-conversion. The angles θ and ϕ used in the tables are measured from the optical z- and x- axes respectively. In Tables 1 and 2, the optical axes are defined so that the refractive indices satisfy $n_x = n_y = n_o > n_z = n_e$, where n_o and n_e are the ordinary and extraordinary refractive indices. In Table 3, the optical axes are defined so that the refractive indices satisfy $n_x < n_y < n_z$. The beam polarizations are denoted by s or p, corresponding respectively to the electric field orthogonal or parallel to the plane containing the propagation direction and the z-axis.

The parameters in the tables were calculated from the refractive index data, thermo-optic data, and nonlinear coefficients presented in [5-8] (BBO), in [4,9] (KD*P), and in [10-13] (LBO). In the case of BBO there are discrepancies in the measured nonlinear coupling quoted in the litera-

ture. In the case of LBO, there are discrepancies in the refractive index data and the thermo-optic data among different authors due to the limited frequency range of their measurements. Data most consistent with other experiments [14] were used here. The temperature dependence of the noncritical phase-matching parameters is not fully consistent with that of the critical phase-matching parameters because the data were taken from different authors [11,13]. The angular tuning parameters in Table 3 for noncritical phase-matching are the measured second-order angular bandwidths.

Beta barium borate is a negative uniaxial material suitable for mixing all the Nd:YAG harmonics in the 213 nm system. Its transmission range is between 196 nm and 2200 nm. It has a relatively strong second-order nonlinearity, high damage threshold, and large temperature acceptance. On the other hand, its angular acceptance is quite small and its thermal conductivity is very poor. The different values of the effective nonlinear coupling d_{eff} in Table 1 correspond to data from references [6] and [8] respectively. Here data from [6] were used in calculations.

Highly deuterated potassium dihydrogen phosphate, also a negative uniaxial material, is a good option for the first two stages of the 213-nm system. It is not capable of generating 213-nm radiation in the third stage because of phase-matching considerations. The transmission range of KD*P is 200 nm to 1500 nm. It has relatively large angular acceptance and reasonably high thermal conductivity. The nonlinear coefficients, damage threshold, and temperature acceptance of KD*P are smaller than those of BBO.

Finally, lithium borate is a biaxial material with transmission range of 160 nm to 2300 nm. Phase-matching is possible in this material only in the first two stages of the quintupler. Noncritically phase-matched doubling of the Nd:YAG frequency is possible with LBO [13]. Although phase matching is possible for most crystal orientations, Table 3 shows only the orientations that result in the strongest nonlinear coupling. This is the orientation with angular tuning in the x-y plane for type I phase-matching and that with angular tuning in the y-z plane for type II phase matching. The effective nonlinearity of LBO is higher than that of KD*P but lower than that of BBO. LBO has large damage threshold and large angular bandwidth but relatively small temperature bandwidth. Its thermal conductivity has not been measured to date.

Other relevant material properties of BBO, KD*P, and LBO are given in Table 4. Since BBO and LBO have only been developed recently, some of their properties have not yet been determined experimentally. The damage threshold data are from [10] and [15]. The damage threshold data are more complete for BBO and KD*P than for LBO. The reported data include a wide range of damage experiments. The lower limits of the data generally correspond to short wavelengths (ultraviolet) and to large number of pulses, while the high values correspond to single pulse measurements and infrared light. The absorption data are from [9], [16], and [17].

TABLE 1. Generation of harmonics of 1064 nm radiation in BBO

frequencies, mixing, polarizations			crystal orientation	d_{eff} [pm/V]	C [$GW^{-1/2}$]	β_θ [cm^{-1}/mrad]	$\Delta\theta L$ [mrad cm]	β_T [cm^{-1}/°C]	$\Delta T L$ [°C cm]	walk-off angles
1+1=2	I	*oo-e*	θ=22.9° ϕ=90°	1.69/2.11	4.07	10.9	0.511	0.155	35.9	- - 3.19°
	II	*eo-e*	θ=32.6° ϕ=0°	1.26/1.80	3.08	7.08	0.786	0.145	38.4	3.76° - 3.95°
1+2=3	I	*oo-e*	θ=31.1° ϕ=90°	1.59/1.98	3.79	21.1	0.263	0.403	13.8	- - 4.08°
	II	*eo-e*	θ=38.2° ϕ=0°	1.10/1.37	2.67	16.0	0.349	0.377	14.8	3.98° - 4.41°
	III	*oe-e*	θ=59.8° ϕ=0°	0.45/0.56	1.12	6.99	0.797	0.342	16.4	- 3.55° 3.73°
2+2=4	I	*oo-e*	θ=47.6° ϕ=90°	1.29/1.62	3.05	33.0	0.169	1.04	5.4	- - 4.77°
	II	*eo-e*	θ=84.7° ϕ=0°	0.03/0.04	0.07	3.15	1.77	0.856	6.5	0.73°- 0.82°
1+4=5	I	*oo-e*	θ=51.1° ϕ=90°	1.21/1.52	2.76	48.0	0.116	1.44	3.9	- - 5.34°
	II	*eo-e*	θ=57.2° ϕ=0°	0.52/0.65	1.22	37.7	0.148	1.31	4.2	3.56°- 4.89°
1+2=3	I	*oo-e*	θ=69.5° ϕ=90°	0.74/0.93	1.73	29.9	0.186	1.95	2.9	- - 3.42°

TABLE 2. Generation of harmonics of 1064 nm radiation in KD*P

frequencies, mixing, polarizations			crystal orientation	d_{eff} [pm/V]	C [$GW^{-1/2}$]	β_θ [cm^{-1}/mrad]	$\Delta\theta L$ [mrad cm]	β_T [cm^{-1}/°C]	$\Delta T L$ [°C cm]	walk-off angles
1+1=2	I	*oo-e*	θ=36.6° ϕ=45°	0.215	0.60	4.47	1.25	0.38	14.7	- - 1.45°
	II	*eo-e*	θ=53.7° ϕ=0°	0.344	0.98	2.41	2.32	0.34	16.4	1.28° - 1.42°
1+2=3	I	*oo-e*	θ=46.8° ϕ=45°	0.263	0.73	7.38	0.755	0.84	6.6	- - 1.59°
	II	*eo-e*	θ=59.5° ϕ=0°	0.315	0.89	4.58	1.22	0.77	7.2	1.17° - 1.38°
2+2=4	I	*oo-e*	θ=86.2° ϕ=45°	0.359	0.99	1.39	3.99	2.02	2.8	- - 0.22°

TABLE 3. Generation of harmonics of 1064 nm radiation in LBO

frequencies, mixing, polarizations			crystal orientation	d_{eff} [pm/V]	C [$GW^{-1/2}$]	β_θ, β_ϕ [cm^{-1}/mrad]	$\Delta\theta L$, $\Delta\phi L$ [mrad cm]	β_T [cm^{-1}/°C]	$\Delta T L$ [°C cm]	walk-off angles
1+1=2	I *xy*	*pp-s*	θ=90° ϕ=11.6°	1.03	2.60	β_ϕ=1.34	4.15	0.96	5.8	- - 0.40°
	II *yz*	*sp-s*	θ=20.5° ϕ=90°	0.84	2.17	β_θ=0.572	9.73	0.90	6.2	- 0.35° -
1+2=3	I *xy*	*pp-s*	θ=90° ϕ=37.1°	0.84	2.10	β_ϕ=5.22	1.07	1.46	3.8	- - 1.04°
	II *yz*	*sp-s*	θ=41.9° ϕ=90°	0.67	1.71	β_θ=1.77	3.15	1.50	3.7	- 0.53° -
1+1=2 NCPM 148 °C	I	*pp-s*	θ=90° ϕ=0°	1.05	2.65	$\beta_\theta^{(2)}$=0.123 $\beta_\phi^{(2)}$=0.090	45.0 61.9	1.43	3.9	- - -

TABLE 4. Properties of BBO, KD*P, and LBO

		β-BaB_2O_4	KD_2PO_4	LiB_3O_5
crystal symmetry		trigonal	tetragonal	orthorhombic
point group		$3m$	$\bar{4}2m$	$mm2$
damage threshold [GW/cm^2]		0.4-50	0.5-10	25
thermal conductivity K [W/cm/°C]		K_{11}=0.0008 K_{33}=0.0080	K_{11}=0.0186 K_{33}=0.0209	not available
fractional thermal expansion [10^{-6}/°C]	α_{11}	4	24.9	33.6
	α_{22}	4	24.9	-88.0
	α_{33}	36	44.0	108.2
density ρ [g/cm^3]		3.849	2.355	2.474
specific heat c, 25°C [J/g/°C]		not available	0.0485	not available
linear absorption α [cm^{-1}]	1064 nm	0.001	α_o=0.002, α_e=0.0004	not available
	532 nm	0.002	0.5	
	355 nm			
	266 nm	0.002	0.02-0.064	
	213 nm			
two-photon absorption β [cm/GW]	355 nm	not available	0.0054	not available
	266 nm		0.027	

3.2 Crystal Geometry Considerations

In most instances of critical phase-matching, the frequency up-conversion process is highly sensitive to angular tuning in one plane only. In uniaxial crystals, this arises from crystal symmetry. In biaxial crystals, the crystal orientation can usually be chosen so that variations in one of the angles, θ or ϕ, are important only to second order. This was done for LBO in Table 3. Since diffraction effects are modeled as effective angular deviations from the phase-matching condition, the harmonic generation process is highly sensitive to the size of the beam in the plane of critical angular tuning. Thus for a given intensity of the input beam, higher efficiency can be achieved with an asymmetric beam cross section. Thus rather than using the traditional design with circular beams and square crystal apertures, elliptical beams and rectangular crystal apertures are considered in this design. In addition, in the rectangular configuration the beam walk-off effect occurs in the plane of the larger dimension. Thus upon exit from the crystal, different harmonics overlap spatially to a larger extent than they would if walk-off occurred in the smaller crystal dimension. A typical crystal configuration is shown in Figure 1. Polarization information relevant to different types of nonlinear mixing is included in the figure. The axes in the figure are used in sections 4 and 5 are not to be confused with the crystal directions defined for crystal symmetry.

FIGURE 1. Nonlinear crystal setup and polarizations

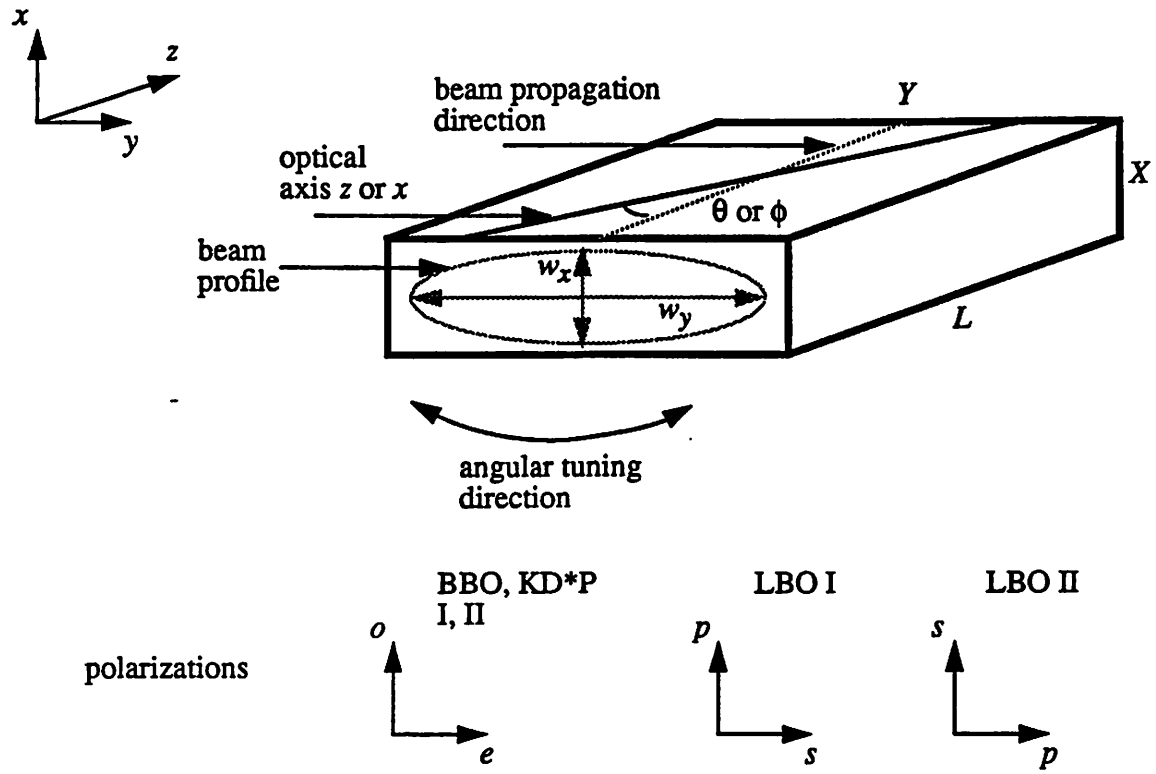

With the slab crystal geometry of Figure 1, heat-sinking is provided to the crystal by thermal contact of the two large crystal facets (top and bottom in figure) with a temperature controlled oven. Practical aspects of providing good thermal contact between the crystal and the oven are discussed in section 6.

3.3 Fifth harmonic generator configuration

In the second generation 213-nm system, the fifth harmonic generator consists of three nonlinear slab-shaped crystals. Its Nd:YAG laser input is a linearly polarized beam with circular cross section. To produce the desired elliptical beam, the incoming beam must be compressed in one dimension before the nonlinear stages. The compression is accomplished with a series of Brewster angle prisms, which are preferable to telescopes because they maintain high beam quality. Telescopes can reduce the beam quality through aberrations in the telescope lenses. Since the input beam is linearly polarized, the prisms are designed to take advantage of no reflection losses for the TM polarization at Brewster's angle of incidence. The TM polarized beam enters each compressing prism at normal incidence and exits at Brewster's angle. Consequently, anti-reflection coatings are required only for the input facet of each prism. When the input beam is at normal incidence, each prism compresses the beam in one dimension by a factor equal to its refractive index. Several prisms can be used in series to produce the desired compression.

Once the beam has the desired cross section, it enters the frequency quintupler. The fifth harmonic can be produced from the pump frequency by two different mixing schemes. Both schemes involve frequency doubling in the first nonlinear stage. One of the schemes then involves doubling of the second harmonic to produce the fourth harmonic in the second stage. The fourth harmonic and the first harmonic left over from the first stage are added in the third stage. As discussed in section 5, this method has lower overall efficiency than the other quintupling scheme, which involves adding the first and second harmonics in the second stage and adding the third and second harmonics in the third stage. The second mixing scheme is the method of choice for the new light source. Each nonlinear crystal of the quintupler requires input beams with specific polarizations and produces uniquely polarized output. The polarization requirements of the $2 + 3 = 5$ mixing scheme are shown in Figure 2 for the three nonlinear stages and various types of nonlinear mixing. The figure would be similar for the $1 + 4 = 5$ mixing scheme.

FIGURE 2. Quintupler polarization requirements

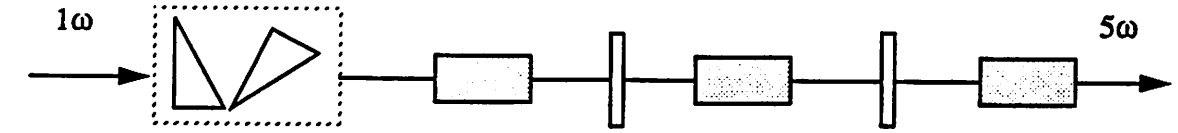

x
y

	compression optics	1st stage		2nd stage		3rd stage	
	input/ output	desired input	output	desired input	output	desired input	output
type I BBO KD*P LBO	1ω	1ω	2ω	1ω 2ω	3ω	2ω 3ω	5ω
type II BBO KD*P		1ω	2ω	2ω 1ω	3ω	2ω 3ω	5ω
type II LBO		1ω	2ω	1ω 2ω	3ω		

The figure shows that for most types of mixing, the output polarizations of one stage do not correspond to polarizations needed in the next stage. As a result, waveplates are required between the different stages to properly reorient the polarizations. For example, if type I mixing in the first nonlinear stage is followed by type II frequency mixer in the second stage, both first and second harmonics must have their polarizations reoriented by 90° after the first stage. This can be accom-

plished with a special multiple-order waveplate. Also when type II mixing crystal is used in the first stage, a quarter-wave plate must precede the first stage. In addition, since the fundamental frequency splits into ordinary and extraordinary components in a type II doubler, the crystal birefringence changes the polarization of the fundamental frequency. Since the fundamental frequency is subsequently used in the second stage, it is desirable to know its polarization after the first stage. However, since nonlinear crystals are strongly birefringent and few centimeters in length, the polarization rotates through several hundred orders during propagation through the crystal. The total polarization change is highly sensitive to temperature and to nonuniformities in the crystal length. As s result, the waveplate needed after the first stage cannot be easily designed and some unknown fraction of the first harmonic energy cannot be used in subsequent stages. Consequently in a multi-stage harmonic generator, type I crystal is preferable to type II crystal in the first stage when the fundamental frequency is used in more than one stage, provided that the type I and the type II frequency mixers have comparable efficiency. For all other types of mixing, suitable waveplates required between the nonlinear stages can be designed.

4.0 Crystal Heating

The fifth harmonic generator consists of nonlinear dielectrics, which generally are poor conductors of heat. Heat supplied to the crystals by absorption cannot be extracted from them very efficiently due to their low thermal conductivity. Since the phase-matching condition is temperature dependent, nonuniform temperature distribution has adverse effects on harmonic conversion efficiency.

4.1 Description of crystal heating

The temperature distribution inside the nonlinear crystal can be calculated from the heat equation and the appropriate boundary conditions. Conduction of heat in a homogeneous, anisotropic solid described by conductivity tensor K_{ij} is described by the equation in time t and position (x, y, z) for the unknown temperature distribution T [18, 19]:

$$\sum_{i,j=1}^{3} K_{ij} \frac{\partial^2 T}{\partial x_i x_j} - \rho c \frac{\partial T}{\partial t} = -A(x, y, z, t), \tag{9}$$

where ρ is the density, c is the specific heat, and $A(x, y, z, t)$ is the heat supplied per unit volume. The subscripts 1, 2, and 3 refer to the directions x, y, and z, respectively.

Although the harmonic generator under consideration operates in pulsed fashion, the crystal heating can be described quite accurately on time-average basis. This can be justified as follows. The characteristic time τ of heat diffusion over some distance x is given by $\tau = x^2/\kappa$, where κ is the heat diffusivity. The heat diffusivity is in turn related to thermal conductivity K, to specific heat c, and to density ρ by the relation $\kappa = K / \rho c$. Using the values of in Table 4, we find that for heat diffusion perpendicular to the optic axis over 0.35 cm in KD*P, the response time is 0.75 seconds. This simple calculation cannot be done for BBO and LBO since their thermal properties have not

yet been measured. However, since thermal conductivity of BBO in the direction of heat extraction is about 20 times smaller than that of KD*P, its response time is expected to be larger. Indeed, its response time was determined previously [1] to be about 15 seconds under similar conditions, which is about 20 times greater than in KD*P. The response times of other dielectric materials, such as LBO, would be expected to have similar order of magnitude. Thus the heat generated in a nonlinear crystal of typical size by absorption of light diffuses from it in time on the order of several seconds. On the other hand, the harmonic generator operates with nanosecond pulses at repetition rate of 1 kHz. Thus the crystal temperature profile is determined by the average absorbed power. Consequently, in the present case, the time dependence in Eq. (9) can be neglected, resulting in the time-averaged heat equation

$$\sum_{i,j=1}^{3} K_{ij} \frac{\partial^2 T}{\partial x_i x_j} = -A(x, y, z), \tag{10}$$

where $A(x, y, z)$ now represents the average power absorbed by the crystal per unit volume. Normal to the propagation direction, the absorbed power is proportional to the transverse beam intensity profile. Along the crystal length the absorbed power varies to some extent because the intensity decreases as the beam propagates through the crystal and because the different harmonic frequencies have different absorption coefficients. According to Table 4 and various references [5, 9, 10], linear absorption coefficients are relatively small at the five Nd:YAG harmonics in the nonlinear materials under consideration. Two-photon absorption in BBO is important at the fourth and fifth harmonic frequencies [20]. However, in the 213-nm system the intensities at the higher harmonics are not expected to be high enough to cause significant two-photon absorption. As a result, the average power absorbed per unit crystal length is taken to be proportional to the intensity. In addition, the energy absorbed per unit length is assumed to be constant, represented by an effective absorption coefficient, even though absorption at the different harmonics may differ.

To determine the boundary conditions in the present design, the crystal geometry shown in Figure 2 is considered. Each crystal has rectangular prism shape, with its top and bottom held at constant temperature T_0 with a temperature-controlled heat sink. The temperature of air in the vicinity of the crystal is assumed to be T_0 as well. The boundary condition at the four crystal sides surrounded by air is given by the fact that the heat flux across the surface equals to the heat loss by conduction, radiation, and convection. This can be expressed as

$$Q_n = L_{conduction} + L_{radiation} + L_{convection}, \tag{11}$$

where Q_n is the heat flux normal to the surface ($Q_i = -K_{ij}\partial T/\partial x_j$). The crystal is surrounded by relatively still air inside its temperature-controlled heat sink. At the crystal-air interfaces, the convection losses are thus negligible and the heat is lost mainly by conduction through the layer of still air. The heat loss is estimated by assuming a constant temperature gradient across the layer of air surrounding the crystal. The heat lost is approximately $L_{conduction} = (K_{air}/d)(T - T_0)$, where $K_{air} = 0.00024$ W/cm/°C is the thermal conductivity of air and d is the air layer thickness. The layer thickness can be taken as part of the distance from the crystal to the edge of the sur-

rounding heat sink, here $d = 0.5$ cm approximately. In general, thermal loss due to radiation is a nonlinear function of temperature. For a body at absolute temperature T in surroundings at temperature T_0, the heat radiated per unit surface area is given by $L_{radiation} = \sigma E (T^4 - T_0^4)$, where σ is the Stefan-Boltzmann constant and E is the surface emissivity. During harmonic generation the crystal temperature is usually only several degrees higher than temperature of the surrounding air, while the absolute crystal temperature is near room temperature. Since the difference between T and T_0 is small compared to T or T_0, the radiative heat loss can be approximated by $L_{radiation} = 4\sigma E T_0^3 (T - T_0)$, with $E \approx 0.75$ and $T_0 = 300$ K. In the case under consideration here, the conduction and the radiation losses are comparable in magnitude, while the convection losses are expected to be negligible in comparison ($L_{convection} \approx 0$). Equation (11) can now be rewritten in terms of an effective coefficient of surface heat transfer H,

$$Q_n = H (T - T_0), \tag{12}$$

where the combined effect of the different heat loss mechanisms is $H = 0.00093$ W/cm^2. This heat loss is relatively small compared to the heat extracted from the crystal by the heat sink.

4.2 Calculation results

The temperature distribution in the nonlinear crystals was determined by numerical solution of the heat equation using the stated assumptions. The partial differential equation was solved by the alternating-direction implicit finite-difference method (ADI) implemented in MATLAB. The calculation determined the temperature distribution in the crystal of given material, shape, phase-matching orientation, and specified absorption profile, oriented and heat sunk as shown in Figure 1. Since the thermal properties of LBO are not known, the calculations could only be done for KD*P and BBO.

Harmonic generation efficiency depends critically on the amount of heat generated by absorption and on the crystal shape. Consequently, it is important to understand how the temperature distribution is influenced by the crystal shape and orientation as well as by absorption. According to (10), for a given crystal and beam shape, the temperature at each point in the crystal increases linearly with the amount of power absorbed. Thus in our simple model of constant absorption per unit length, temperature increases in proportion to total average power. It is also evident from (10) that the temperature remains unchanged when all the crystal and transverse beam dimensions are changed by a given factor. Consequently, only the relative crystal shape and size with respect to the beam size determines the temperature distribution.

Although the heat problem is relatively complex due to crystal anisotropy and nonuniform absorption, some simple facts can be deduced about its solutions. Since the heat is extracted from the slab-shaped crystal in the x-direction (see Figure 1), the shape of the crystal input aperture and the transverse beam profile strongly affect the temperature distribution. To utilize the crystal most efficiently with minimal heating, the beam size should approximately match the input aperture of the crystal, so that while most of the beam energy enters the crystal, the heat diffuses over shortest possible distance. At a given absorption level, heating is smallest for thin crystals. For input aper-

tures with large aspect ratios, the temperature decreases approximately in proportion to the inverse aspect ratio *X/Y* because the heat flow in the *y*-direction is negligible. When the aspect ratio is of order unity, the temperature decreases more slowly with increasing aspect ratio. In addition, the temperature is a relatively weak function of the crystal length because most heat flows in the *x*-*y* plane. When crystal length is comparable to transverse crystal dimensions, less of the generated heat exits the input and output crystal facets for a longer crystals than for shorter crystals. Thus temperature slowly increases with length, eventually reaching a constant value for very long crystals. Finally, the temperature depends on the crystal orientation. In a particular uniaxial material, the differently oriented crystals have different thermal conductivities in the *y*-*z* plane but identical conductivities in the *x*-direction. Thus even though the crystal orientation affects the spatial temperature distribution, the temperature difference between the crystal center and the heat sink is not strongly dependent on the crystal orientation in BBO and KD*P. This would is not the case in biaxial crystals, where the different crystal orientations would have different thermal conductivities in the *x*-direction. The dependence of conversion efficiency on heating is discussed in section 5.

An example of calculated results is shown in Figure 3. The figure shows the temperature distribution in a crystal suitable for the first stage of the fifth harmonic generator, BBO type I doubler. The calculation was done for absorbed power, crystal shape, and input beam profile dimensions indicated in the figure. The figure shows the temperature for three cross sections through the crystal center, indicated on the schematic, as well as the absorption profile in the *x*-*y* plane. The generated heat $A(x, y)$ was taken to be proportional to the input beam intensity profile, determined by the characteristics of the Nd:YAG laser pump. The Nd:YAG laser used in the second generation 213-nm light source consists of unstable resonator cavity with output coupling around one the mirrors. The output coupler is a soft-edged mirror, which produces annular shaped output beam. Before the beam enters the harmonic generator, it is compressed in one dimension. This results in the following input beam intensity profile [2]:

$$I(x,y) = I_0 \exp\left(-2\left(\frac{x^2}{w_x^2}+\frac{y^2}{w_y^2}\right)^{5/2}\right)\left(1-0.74\exp\left(-2\left(\frac{(1.5x)^2}{w_x^2}+\frac{(1.5y)^2}{w_y^2}\right)^{5/2}\right)\right). \quad (13)$$

It is evident from Figure 3 that the temperature distribution is strongly influenced by the absorption profile. Like the intensity profile, the temperature distribution has two peaks in the *y*-direction, where the heat flow is small. Along *x*-axis, the direction of heat extraction, the temperature is maximum at the center. The temperature is nearly uniform in the *z*-direction, since the absorption is uniform by assumption. The figure also shows that in *y*-*z* plane, the heat flows primarily along the direction of the optic axis, where the thermal conductivity is the greatest.

FIGURE 3. Temperature distribution in BBO I crystal for doubling 1064-nm radiation

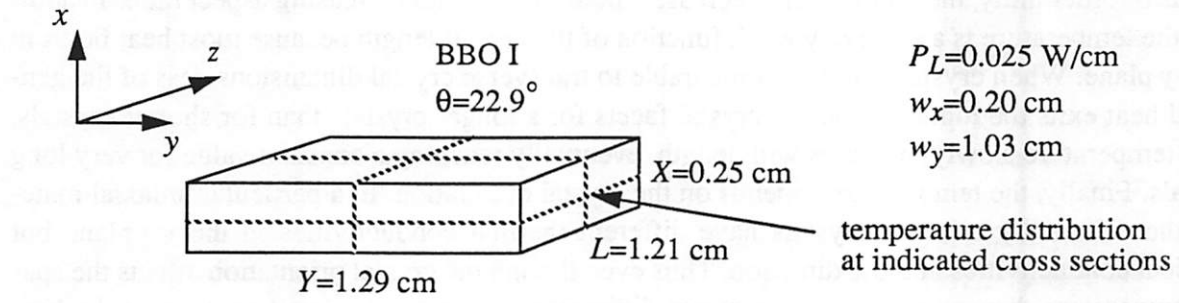

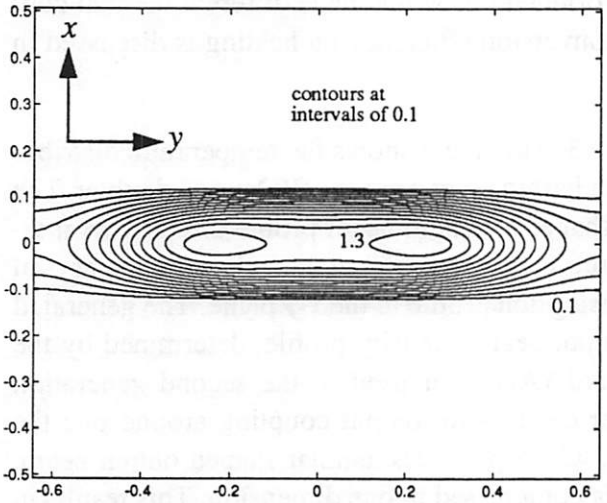

x-y plane temperature distribution [°C]

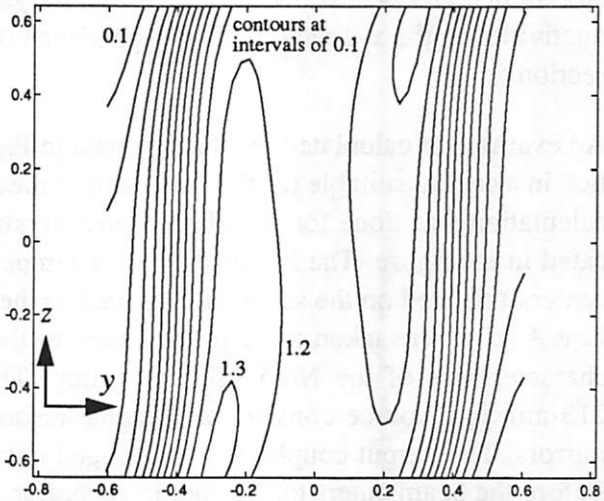

y-z plane temperature distribution [°C]

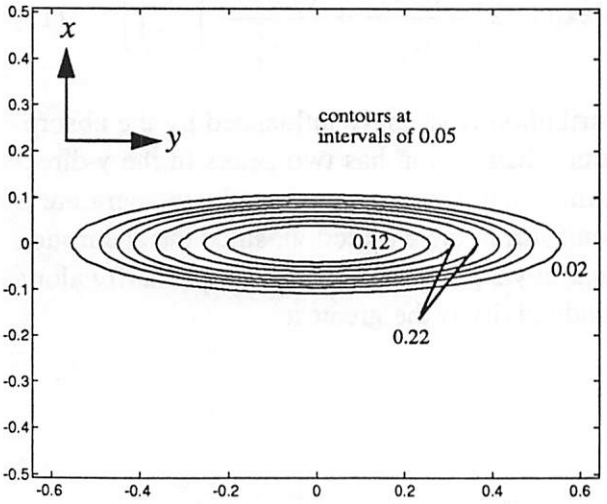

absorption profile $A(x, y)$ [W/cm^3]

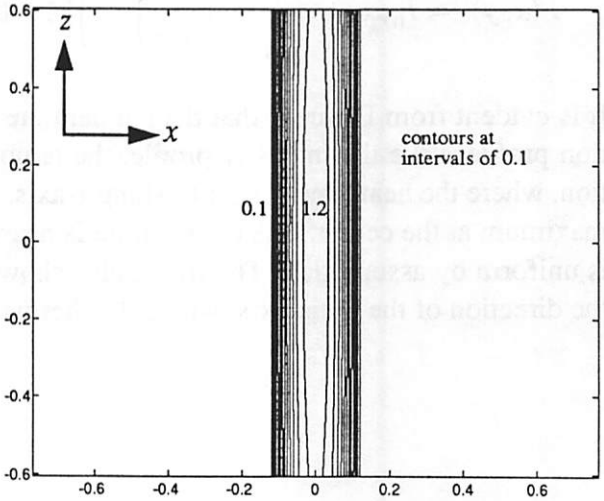

x-z plane temperature distribution [°C]

5.0 Conversion Efficiency

The main goal of the harmonic generator design is to produce the 213-nm radiation with the highest possible conversion efficiency. The conversion efficiency of second harmonic generation (SHG) and of sum-frequency generation (SFG) in the context of the frequency quintupler is the topic of this section.

5.1 Derivation of conversion efficiency

Equations that describe frequency doubling (2) and sum-frequency generation (4) can be solved analytically for the case of lossless media with all absorption coefficients equal to zero [22]. The solutions involve Jacobian elliptic functions. Solutions shown here are for the case of no input at the sum frequency, applicable to the 213-nm system.

Considering frequency doubling with input intensity I_1 at frequency ω and no input at the second harmonic frequency 2ω, the intensity of the second harmonic wave after propagation through a nonlinear crystal of length L is given by

$$I_2(L) = U_b^2 \,\mathrm{sn}^2\left(CLU_c \middle| \frac{U_b^2}{U_c^2}\right) \tag{14}$$

where U_b and U_c are defined by

$$U_c^2,\ U_b^2 = I_1 + \frac{1}{2}\left(\frac{\Delta k}{2C}\right)^2 \pm \sqrt{\left(I_1 + \frac{1}{2}\left(\frac{\Delta k}{2C}\right)^2\right)^2 - I_1^2}. \tag{15}$$

Conventions of reference [23] for the Jacobian elliptic function $\mathrm{sn}(u|\, m)$ are used. Similarly, the solution for sum-frequency generation, when no input at the sum-frequency $c\omega$ is present and the input intensities at frequencies $a\omega$ and $b\omega$ are I_1 and I_2, is

$$I_3(L) = V_b^2 \,\mathrm{sn}^2\left(\sqrt{ab}CLV_c \middle| \frac{V_b^2}{V_c^2}\right) \tag{16}$$

with V_b and V_c defined by

$$V_c^2,\ V_b^2 = \frac{1}{ab}\left[\frac{cbI_1}{2} + \frac{caI_2}{2} + \frac{1}{2}\left(\frac{\Delta k}{2C}\right)^2 \pm \sqrt{\left(\frac{cbI_1}{2} + \frac{caI_2}{2} + \frac{1}{2}\left(\frac{\Delta k}{2C}\right)^2\right)^2 - c^2abI_1I_2}\right]. \tag{17}$$

For the analysis of highly efficient frequency up-conversion it is convenient to represent the solution in terms of dimensionless variables. For the case of second harmonic generation, they are defined as follows [4]:

$$\eta_0 = C^2 L^2 I_1, \tag{18a}$$

$$\delta = \frac{\Delta k L}{2}. \tag{18b}$$

The nonlinear drive η_0 is a measure of the interaction strength over the crystal length and the dephasing δ indicates the amount of phase mismatch. Using these definitions, the conversion efficiency of second harmonic generation becomes [4]

$$\eta_{SHG} = \frac{I_2(L)}{I_1} = \tanh^2\left(\frac{1}{2}\operatorname{atanh}\left(\operatorname{sn}\left(2\sqrt{\eta_0}\,\middle|\,1+\frac{\delta^2}{4\eta_0}\right)\right)\right). \tag{19}$$

This analysis is extended here for sum-frequency generation, which is more complicated because it involves two input beams. The appropriate dimensionless drive variables, proportional to the input intensities I_1 and I_2, are

$$\eta_1 = cbC^2 L^2 I_1, \tag{20a}$$

$$\eta_2 = caC^2 L^2 I_2. \tag{20b}$$

The definition of the dephasing δ for sum-frequency generation is the same as Eq. (18b). Conversion efficiency of sum-frequency generation is subsequently obtained with the use of these definitions and of the descending Landen transformation for the Jacobian elliptic functions [23].

$$\eta_{SFG} = \frac{I_3(L)}{I_1 + I_2} = \frac{\sqrt{\eta_1 \eta_2}}{\frac{a}{c}\eta_1 + \frac{b}{c}\eta_2} \times \tanh^2\left(\frac{1}{2}\operatorname{atanh}\left(\operatorname{sn}\left(2\sqrt{\eta_1\eta_2}\,\middle|\,1+\frac{\delta^2 + (\sqrt{\eta_1} - \sqrt{\eta_2})^2}{4\sqrt{\eta_1\eta_2}}\right)\right)\right) \tag{21}$$

Sum-frequency conversion efficiency η_{SFG} reduces to the simpler frequency doubling form η_{SHG}, provided that the condition $\eta_1 = \eta_2$, or equivalently $I_1/a = I_2/b$, is satisfied. This corresponds to the case when the input number of photons at frequency $a\omega$ is equal to the input number of photons at frequency $b\omega$. Observation of the form of the SFG efficiency indicates that mismatch in the input photon numbers is similar to an increase in the dephasing. Physically this means that the frequency up-conversion cannot continue after one of the input beams is depleted and the energy is converted back into the fundamental waves instead.

5.2 Beam and crystal geometry

In the case of second harmonic generation, the best efficiencies can be achieved when the dephasing is small ($\delta << \pi/10$) and the drive is relatively small but greater than unity ($1 < \eta_0 < 5$). Although the efficiency can be quite large for other drive-dephasing regions ($\delta = 1.5 \pm \pi/10$, $15 < \eta_0 < 40$), operation under those conditions is less advantageous because the efficiency is

high only for spatially and temporally flat beam profiles and very low for the low-intensity beam edges [4]. In reality, the beam profile is not exactly constant in time or uniform within the beam area. Thus for real optical beams, the best efficiency is achieved when the dephasing is small and the temporal and spatial beam edges experience at least moderate efficiency of frequency up-conversion. In the case of sum-frequency generation, it is also desirable for the dephasing to be small. Comparison of (19) and (21) shows that the geometric mean of the two drives η_1 and η_2 for SFG is effectively equivalent to the drive η_0 of SHG. Thus the highest efficiency is possible when $\sqrt{\eta_1\eta_2}$ is greater than unity but not too large. However, high conversion efficiency also requires that both drives η_1 and η_2 be approximately equal.

Drive and dephasing depend on the beam characteristics as well as on the geometry of the crystal. The optical beam in the three-stage colinear 213 nm system is nearly diffraction-limited. The beam is characterized by its peak power and by its transverse profile and dimensions. Assuming the beam size is w_x in the sensitive angular tuning direction and in the other direction it is w_y, the drive parameters in (18) and (20) can be rewritten for both SHG and SFG as

$$\eta_0 = \frac{C^2L^2P_0}{w_xw_y}, \tag{22a}$$

$$\eta_1 = \frac{caC^2L^2P_1}{w_xw_y}, \tag{22b}$$

$$\eta_2 = \frac{caC^2L^2P_2}{w_xw_y}, \tag{22c}$$

where P_0, P_1, and P_2 are the peak input powers in each case. According to Eq. (8), the dephasing parameter depends on diffraction of the beam and on the crystal temperature profile. Diffraction effects can be modeled by assuming that the finite divergence of the interacting beams results in an effective angular deviation from the phase-matching condition [4]. Since the crystal is sensitive to angular tuning only in one dimension, only diffraction in that dimension affects phase matching. The effective phase mismatch is thus proportional to the diffraction limit of beam divergence, or equivalently to the ratio of wavelength and beam size in the critical tuning direction. Empirically, the deviations from the diffraction limit may be modeled by introducing so-called beam quality factor Q. Unity quality factor represents the diffraction limit, while larger factor indicates deviations from the diffraction limit. The angular dephasing can thus be written as

$$\delta_{angular} = \frac{1}{2}\beta_\theta\lambda Q\frac{L}{w_y}. \tag{23}$$

Similarly, temperature nonuniformities in the crystal are modeled as thermal deviations from the phase matching condition. The difference in temperature between inside of the crystal and the heat sink is a measure of the amount of thermal dephasing. Under conditions described in section 4, when the aspect ratio of the crystal aperture is large, the temperature difference ΔT is

approximately proportional to the transverse crystal dimensions ratio X/Y, which is equal to w_x/w_y when the ratios w_x/X and w_y/Y are fixed. Also when the crystal length is large in comparison to transverse dimensions, the temperature difference is approximately independent of length L. Finally, the temperature difference is proportional to the power absorbed per unit length P_L. Thus thermal dephasing is given by

$$\delta_{thermal} = \frac{1}{2}\beta_T P_L F\left(K, X, Y, L, \theta, \phi, A\left(x, y\right)\right)\frac{w_x}{w_y}L, \tag{24}$$

where the factor F depends on the thermal conductivity tensor, on the crystal shape and orientation, and on the absorption profile. In the limiting case of long crystals and apertures with large aspect ratios, the factor F is approximately constant for a given crystal shape and orientation and particular beam profile. Equations (23) and (24) are combined to give the total dephasing:

$$\delta = \delta_{thermal} + \delta_{angular}. \tag{25}$$

5.3 Optimizing crystal shape

In the harmonic generator design, most parameters are determined by properties of the laser pump and by nonlinear material characteristics. Only the crystal shape and the beam size are chosen in the design process. The transverse beam dimensions can be changed with prisms or telescopes, so the crystal and beam dimensions are chosen to ultimately result in the best possible conversion efficiency. First transverse beam and crystal dimensions are determined so that diffraction and heating effects are minimized. Subsequently, the optimum crystal length is found.

Transverse beam and crystal dimensions are chosen to obtain highest efficiency under the constraints of the overall three-stage system. To determine the optimum input aperture of the crystal, let us first consider the effect of input aperture aspect ratio on efficiency. According to Eq. (22), changing the aspect ratio w_y/w_x has no effect on the drive, when the beam area is kept constant. On the other hand, dephasing in Eqs. (23) and (24) is profoundly affected by the aspect ratio of the input beam size. At fixed intensity, both angular and thermal contributions to the dephasing are minimized when the aspect ratio w_y/w_x is maximum. Since small dephasing is desirable for high conversion efficiencies, the maximum possible aspect ratio of the crystal input aperture is the best choice. Considering the case when beam dimension w_x is fixed and w_y is varied, one might think that smaller aspect ratio would produce larger intensity, which would increase the drive and the efficiency. However, like the drive, the dephasing also increases by the same factor. In addition the optimum crystal length also changes. Overall, within the operating range of interest here, a smaller aspect ratio results in decreased efficiency.

The optimum crystal size may be deduced as follows. Let us assume that the beam size can be changed at will by telescoping and that the crystal size relative to the beam size remains constant. When all dimensions of a given crystal are increased by some factor m, the drive is unchanged but

the dephasing changes. While the contribution of diffraction to dephasing stays the same, the contribution of temperature nonuniformities increases in proportion to m. In the second generation 213-nm system with high average power, thermal dephasing is significant. Since large dephasing is detrimental to the conversion process, use of crystals as small as possible leads to highest conversion efficiency.

In a multi-stage system with several nonlinear crystals enclosed in heat sinks and with the necessary waveplates, the minimum crystal size is limited by diffraction effects. In order to maintain high peak powers and good beam quality in the entire system, it is imperative that the beam size stay nearly constant as the beam passes through the system. In the 213-nm system, the transverse beam size should be at least 0.2 cm to achieve negligible diffraction over its length of 20-30 cm. The diffraction effects considered here are those of nearly diffraction-limited input beam at the 1064-nm wavelength. Smaller beam size could be used if refocusing optics were used between the different nonlinear stages. However, this case will not be considered here.

The larger beam dimension is determined by properties of the beam compression optics preceding the nonlinear crystals. Each compression prism increases the aspect ratio of the beam by a factor equal to its refractive index. One, two, three, and four prisms made of BK7 glass increase the aspect ratio by factors of 1.51, 2.27, 3.42, and 5.15, respectively. Since a large aspect ratio is advantageous, it is desirable to use four prisms for beam compression, resulting in 1.03-cm beam size along the larger dimension. Use of even larger aspect ratios requires relatively large crystals, exceeding commonly available sizes.

The last parameter to be determined is the ratio of beam size to size of the crystal aperture. For the most efficient use of the nonlinear material with minimal heating, the beam should just fill the crystal. Thus the crystal aperture should have roughly the same size as the beam. In this design, the beam size is chosen to fit the clear aperture of the crystal so that the beam is incident only on the properly polished and anti-reflection coated part of the crystal facet. The clear aperture is typically 80% of each linear dimension of the crystal facet. With the chosen beam size, the crystal aperture dimensions are $X = 0.25$ cm and $Y = 1.29$ cm.

After the transverse size and dimensions are determined, the optimum crystal length is found. The optimum length depends on peak intensity, diffraction of the beam, and crystal heating. Peak intensity and diffraction are given by the shape and spatial profile of the beam as well as by the energy and duration of the laser pulses. On the other hand, the temperature depends on the amount of absorbed power and on the crystal length. The average power absorbed per unit length may also depend on conversion efficiency when the different harmonics have different absorption constants. In general, the optimum crystal length must be found in several iterative steps. First, the amount of temperature dephasing is estimated. Subsequently, the optimum crystal length is found with use of Eqs. (19) or (21). Then the temperature distribution is calculated by solving the heat equation. The temperature difference within the crystal is then used in the next efficiency calculation to find the optimum crystal length. The entire process is repeated until the crystal length, the amount of heating, and the thermal dephasing are all mutually consistent.

5.4 Results

The conversion efficiency of each stage is a function of many variables, which are determined by the properties of the laser pump. The properties of the present 213-nm light source and the second generation design are summarized in Table 5. Compared to the first generation system, the new source would be more suitable for lithography applications because of its higher repetition rate, smaller pulse energies, and larger average power output. The highly coherent output of both systems produces speckle noise. To achieve the required resist exposure uniformity, the speckle contrast must be averaged out by using many pulses for exposure, even with the help of speckle reduction optics [1]. Since the number of pulses required for averaging is fixed, less energy is used in speckle reduction with low energy pulses than with high energy pulses. In addition, higher average power produced by the new system allows greater throughput. Since the new system also has lower peak intensities, it is less likely that its optical components will be damaged. Finally, the lower peak intensities at the fourth and fifth harmonics result in negligible two-photon absorption. The drawback of smaller pulse energies is reduced conversion efficiency. As a result, pulse compression with stimulated Brillouin scattering (SBS) is needed to boost the peak powers to maintain high conversion efficiency. In the new design, the peak powers are still somewhat smaller than in the first generation system, leading to smaller overall conversion efficiency.

TABLE 5. 213 nm light source parameters

		Present System	New Design before SBS	New Design after SBS
repetition rate	[Hz]	10	1000	1000
beam diameter	[cm]	0.5	0.45	0.2 x 1.03
pulse duration	[ns]	8	15	2
pulse energy at 1064 nm	[mJ]	410	15-50	10-35
total average power at 1064 nm	[W]	4.1	15-50	10-35
peak intensity at 1064 nm	[MW/cm^2]	260	47-157	31-108
average power at 213 nm	[W]	0.05-0.25	--	0.1-1.2

The goal of this design is to find the optimum crystal shapes for the three-stage fifth harmonic generator. Although most of the important parameters are determined by laser properties and choice of beam size, it is desirable for the generator to be efficient when some parameters are unknown or subject to change. For example, one may want to be able to adjust the output power from the system by changing the laser pulse energy. Also the beam quality may be difficult to determine. Both changes in pulse energy and beam quality affect the optimum crystal length. Here the crystal design includes a range of operating conditions. The input at 1064 nm to the harmonic generator is expected to be 10-35 W of average power, with typical operation in the 10-20 W range. The beam quality is expected to be nearly diffraction limited, so the beam quality factor used includes Q = 1-1.5 range. For all nonlinear stages, the wavelength used to determine the dif-

fraction effects was the pump wavelength because the generated harmonics originate from the pump beam. Also, beam walkoff was neglected in these calculations. Other parameters used in the calculations are listed in Table 5.

The effect of crystal heating evaluated in the optimization process depends critically on crystal absorption coefficients. Table 4 contains currently available absorption data for BBO and KD*P. From these data, reasonable estimates of absorption at all wavelengths of interest were made. The absorption at 1064 nm, 532 nm, 355 nm, 266 nm, and 213 nm for BBO was taken to be 0.1 %/cm, 0.2 %/cm, 0.2 %/cm, 0.2 %/cm, and 1 %/cm, respectively. For KD*P, the absorption at the first four harmonics was assumed to be 0.2 %/cm, 0.5 %/cm, 0.5 %/cm, and 3 %/cm. Two-photon absorption was neglected because the peak intensities at fourth and fifth harmonics are not large in this design. Since only a small fraction of the beam energy is absorbed in the crystals, absorption effects were neglected in the efficiency calculations. The average power absorbed per unit length, assumed to be uniform, was determined iteratively during the optimization from the efficiency of each crystal. The beam profile of Eq. (13) was used to determine the heating effects but was not used in the efficiency calculations. The different intensity levels in the beam require different crystal lengths for maximum conversion efficiency. In practice, each nonlinear crystal must have a fixed length. Consequently, calculations were done with a uniform beam profile of elliptical cross section with dimensions listed in Table 5, so that a single crystal length could be determined. The optimum length found for the averaged intensity results in high conversion efficiency for most parts of the beam, though not as high as when the crystal length could fit the beam intensity profile.

FIGURE 4. Efficiency and optimum crystal length of BBO I crystal for doubling 1064 nm

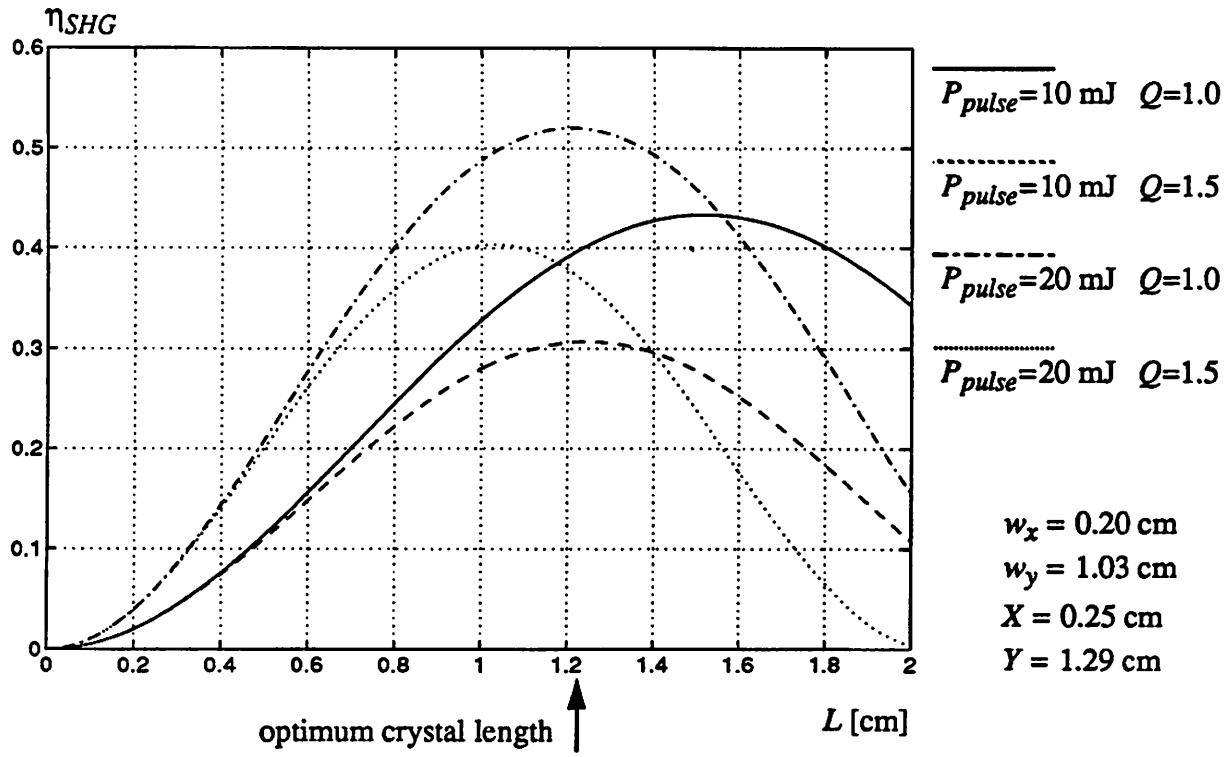

The optimum crystal lengths and conversion efficiencies are listed in Tables 6-10. Results are shown for different types of nonlinear crystals suitable for the different stages of the harmonic generator. The efficiencies of the second and third stages were calculated after crystals appropriate for the preceding stages and their efficiencies were determined. The optimum lengths and maximum efficiencies for the above mentioned range of operating conditions are included. Since only one crystal is used in practice, the crystal length must be chosen to produce high conversion efficiency under a variety of operating conditions. The efficiency versus length curves for several operating conditions are shown in Figure 4. As shown in the figure, the optimum length variations are not great for operating conditions of interest. The crystal length that produces highest overall efficiency, is indicated in the figure.

TABLE 6. 2 x 1064 nm : optimum crystal lengths and maximum efficiencies

nonlinear crystal	input power P_{AVG} [W]	absorbed power P_L [W/cm^{-1}]	beam quality Q	ΔT [°C]	optimum length L [cm]	maximum efficiency [%]
BBO I	10	0.0122	1	0.69	1.52	43
	10	0.0115	1.5	0.65	1.25	31
	20	0.0252	1	1.43	1.21	52
	20	0.0240	1.5	1.36	1.03	40
BBO II	10	0.0124	1	0.70	2.12	47
	10	0.0117	1.5	0.66	1.77	35
	20	0.0255	1	1.44	1.65	55
	20	0.0244	1.5	1.37	1.43	44
KD*P I	10	0.0221	1	0.055	5.62	14
	10	0.0211	1.5	0.052	4.08	7.6
	20	0.0465	1	0.115	4.93	22
	20	0.0438	1.5	0.108	3.75	13
KD*P II	10	0.0270	1	0.066	6.60	46
	10	0.0250	1.5	0.062	5.46	34
	20	0.0565	1	0.139	5.23	55
	20	0.0530	1.5	0.131	4.48	43
LBO I	10	-	1	0.70-0.055	2.35-3.98	42-81
	10	-	1.5	0.66-0.052	2.31-3.65	41-75
	20	-	1	1.44-0.115	1.47-2.88	34-82
	20	-	1.5	1.37-0.108	1.43-2.71	33-79
LBO II	10	-	1	0.70-0.055	2.79-5.27	42-87
	10	-	1.5	0.66-0.052	2.80-4.98	42-84
	20	-	1	1.44-0.115	1.70-3.68	32-86
	20	-	1.5	1.37-0.108	1.67-3.55	31-84

TABLE 7. 1064 nm + 532 nm : optimum crystal lengths and maximum efficiencies

nonlinear crystal	input power P_{AVG} [W]	absorbed power P_L [W/cm^{-1}]	beam quality Q	ΔT [°C]	optimum length L [cm]	maximum efficiency [%]
BBO I	10	0.0144	1	0.80	0.86	28
	10	0.0133	1.5	0.74	0.69	16
	20	0.0316	1	1.76	0.70	37
	20	0.0283	1.5	1.57	0.57	25
BBO II	10	0.0144	1	0.80	1.16	25
	10	0.0133	1.5	0.73	0.92	14
	20	0.0315	1	1.74	0.93	33
	20	0.0282	1.5	1.56	0.77	22
KD*P I	10	0.0325	1	0.080	3.17	14
	10	0.0295	1.5	0.073	2.36	7.1
	20	0.0734	1	0.181	2.72	22
	20	0.0638	1.5	0.157	2.11	13
KD*P II	10	0.0333	1	0.082	3.84	30
	10	0.0301	1.5	0.074	3.09	18
	20	0.0752	1	0.185	3.13	40
	20	0.0652	1.5	0.161	2.57	27
LBO I	10	-	1	0.80-0.080	1.38-2.07	22-46
	10	-	1.5	0.74-0.073	1.27-1.79	17-32
	20	-	1	1.76-0.181	0.95-1.67	17-58
	20	-	1.5	1.57-0.157	0.83-1.41	16-42
LBO II	10	-	1	0.80-0.080	1.70-2.82	22-54
	10	-	1.5	0.74-0.073	1.67-2.53	19-41
	20	-	1	1.76-0.181	0.95-2.25	15-66
	20	-	1.5	1.57-0.157	0.99-1.92	15-50

TABLE 8. 2 x 532 nm : optimum crystal lengths and maximum efficiencies

nonlinear crystal	input power P_{AVG} [W]	absorbed power P_L [W/cm^{-1}]	beam quality Q	ΔT [°C]	optimum length L [cm]	maximum efficiency [%]
BBO I	10	0.0139	1	0.75	0.73	2.5
	10	0.0131	1.5	0.70	0.53	1.0
	20	0.0304	1	1.63	0.59	4.2
	20	0.0275	1.5	1.47	0.46	1.9
KD*P I	10	0.0430	1	0.105	6.89	23
	10	0.0356	1.5	0.087	6.70	17
	20	0.0977	1	0.240	4.02	20
	20	0.0787	1.5	0.193	4.32	17

TABLE 9. 1064 nm + 266 nm : optimum crystal lengths and maximum efficiencies

nonlinear crystal	input power P_{AVG} [W]	absorbed power P_L [W/cm^{-1}]	beam quality Q	ΔT [°C]	optimum length L [cm]	maximum efficiency [%]
BBO I	10	0.0148	1	0.78	0.45	3.1
	10	0.0134	1.5	0.70	0.34	1.1
	20	0.0328	1	1.72	0.37	5.1
	20	0.0288	1.5	1.49	0.29	2.3
BBO II	10	0.0143	1	0.74	0.62	1.1
	10	0.0132	1.5	0.68	0.45	0.39
	20	0.0313	1	1.62	0.50	1.8
	20	0.0280	1.5	1.44	0.39	0.81

TABLE 10. 532 nm + 355 nm : optimum crystal lengths and maximum efficiencies

nonlinear crystal	input power P_{AVG} [W]	absorbed power P_L [W/cm^{-1}]	beam quality Q	ΔT [°C]	optimum length L [cm]	maximum efficiency [%]
BBO I	10	0.0158	1	0.77	0.65	4.7
	10	0.0140	1.5	0.68	0.52	2.3
	20	0.0362	1	1.77	0.45	5.9
	20	0.0304	1.5	1.48	0.40	3.5

The choice of crystal most appropriate for each nonlinear stage is evident from Tables 6-10. For the first-stage doubler, a type I phase-matching is most suitable because the polarization of the first harmonic must be known before it is used in subsequent stages. Due to crystal birefringence, type II doubling changes the polarization of the first harmonic and heating effects make it difficult to determine the output polarization. Thus a type I mixing is preferred to a type II mixing in the first stage, even when its efficiency is somewhat lower. Thus the best option for the first doubling stage is a BBO crystal, oriented for type I phase-matching. Critically or noncritically phase-matched type I doubling in an LBO crystal may be even more efficient. However, LBO is not widely available at present and some of its properties are not well known. Its efficiency and optimum length cannot be found accurately because its absorption and thermal properties are not known. Since the transmission range of LBO is greater than that of BBO and KD*P, its absorption is expected to be smaller that of BBO and KD*P. Tables 6 and 7 show the efficiencies of LBO with the same thermal dephasing as BBO and KD*P. BBO and KD*P were chosen as reasonable limits of thermal dephasing, since thermal conductivity of KD*P is relatively large and that of BBO is relatively small.

After the first nonlinear stage, two frequency-mixing options for producing the fifth harmonic exist. One scheme involves adding the first and second harmonics in the second stage and second

and third harmonics in the last stage. With this mixing scheme, KD*P crystal for type II frequency mixing is a good option for the second nonlinear stage. Once again, LBO appears to be a good option for this mixing stage. In the last stage, only a BBO crystal oriented for type I phase matching has enough birefringence to be capable of mixing second and third Nd:YAG harmonics. With the alternative mixing scheme, the second harmonic is doubled in the second stage and the first and fourth harmonics are added in the third stage. With the low peak intensities present in this system, the only good option for the second stage is a type I mixing KD*P crystal. Finally, type I mixing BBO crystal is appropriate for the third stage. Both mixing schemes require waveplates between the first and the second stages and between the second and the third stages to properly reorient the polarizations of the interacting waves.

In this 213 nm system, the efficiencies of individual nonlinear stages are relatively low because peak intensities are not exceptionally high and heating effects are sizable. The heating is not very large in the first nonlinear stage but significantly decreases efficiencies in the second and third stages. Heating is smaller in the first stage crystal because the lower harmonic frequencies experience less absorption and first-stage crystals have larger thermal bandwidths than crystals for subsequent stages. On the other hand, absorption and thermal bandwidths are less favorable for harmonic conversion in the latter stages. Thermal dephasing is most significant in the third stage, where it can reduce the efficiency by a large factor, compared to the case when heating is not present. Due to the high repetition rate and high average power of the system, peak intensities cannot become large and heating cannot be avoided. The performance could only be enhanced by decreasing the beam and crystal size in order to increase intensities and improve heat extraction. Due to diffraction limitations these improvements are possible only with additional optical components between the nonlinear stages.

TABLE 11. 2 + 3 = 5 mixing scheme: optimum crystal lengths and efficiencies

input power P_{AVG} [W]	beam quality Q	1+1 stage	L [cm]	eff [%]	1+2 stage	L [cm]	eff [%]	2+3 stage	L [cm]	eff [%]	overall efficiency [%]
10	1			39.4			27.2			3.96	1.92
10	1.5	BBO	1.21	30.6	KD*P	3.06	17.8	BBO	0.48	2.23	0.815
20	1	type I		52.0	type II		40.2	type I		5.87	3.84
20	1.5			37.6			24.5			3.16	1.45

TABLE 12. 1 + 4 = 5 mixing scheme: optimum crystal lengths and efficiencies

input power P_{AVG} [W]	beam quality Q	1+1 stage	L [cm]	eff [%]	2+2 stage	L [cm]	eff [%]	1+4 stage	L [cm]	eff [%]	overall efficiency [%]
10	1			39.4			18.1			2.80	1.90
10	1.5	BBO	1.22	30.6	KD*P	4.85	13.9	BBO	0.36	1.11	0.818
20	1	type I		52.0	type I		18.3	type I		5.06	2.91
20	1.5			37.6			16.5			1.99	1.37

The best crystal options and their efficiencies are shown in Tables 11 and 12 for both mixing schemes. Clearly the scheme of choice for the second generation 213-nm light source for lithography is the 2 + 3 = 5 mixing scheme because it is capable of higher overall efficiency than the alternative 1 + 4 = 5 mixing scheme. In both mixing schemes, some harmonics are used as inputs in more than one nonlinear stage. In the 1 + 4 = 5 scheme, the first harmonic is used in the first and the last stage. In the 2 + 3 = 5 mixing scheme, the first harmonic is used in the first and second stages and the second harmonic is used in the second and the third stage. It is important to consider that these frequencies might be depleted in one crystal, causing photon mismatch and lower efficiency in the following crystal. To illustrate this, it is useful to consider full conversion from the fundamental to the fifth harmonic. In the 2 + 3 = 5 mixing scheme the ideal efficiencies of the first, second, and third stages, as defined in Eqs. (19) and (21), are respectively 80%, 60%, and 100%. Thus the first stage converts most of the power to the second harmonic but enough power is left over to be used in the second stage. Similarly, the second stage converts all of the first harmonic and only some of the second harmonic to the third harmonic, producing beams with matched photon numbers as input for the last stage. With the 1 + 4 = 5 mixing scheme, three nonlinear stages producing full conversion to the fifth harmonic have ideal efficiencies of 80%, 100%, and 100% respectively. These idealized efficiencies are useful because they indicate that the first harmonic beam will not be depleted for use in later stages unless the first stage efficiency exceeds 80% for both mixing schemes. In the 2 + 3 = 5 mixing scheme, the second harmonic can be depleted in the second stage. The optimum efficiency for preventing depletion depends on the efficiency of the first stage. For example, when the first stage is 50% efficient, the efficiency of the second stage should not exceed 45% to avoid depletion of the second harmonic beam. In the new 213-nm system, the efficiencies are not high enough for depletion effects to be important.

6.0 Experimental Results

To assess the performance of the new crystal geometry, a slab-shaped crystal was tested in the first generation 213-nm system. The conversion efficiency of the slab geometry crystal was measured and compared to calculations. In addition, a simple method to determine the crystal temperature during harmonic conversion was tested.

6.1 Conversion efficiency measurements

A slab-shaped BBO crystal is used as the third nonlinear stage that produces 213-nm radiation from its 532-nm and 355-nm inputs in our first generation harmonic generator. The setup is shown in Figure 5. The beam exiting the second stage of the harmonic generator enters either the conventional square-aperture crystal or is redirected with the help of a turning prism to the slab-shaped crystal. The slab-shaped crystal is preceded by a cylindrical lens telescope that compresses the beam in one dimension by a factor of 3.3 to produce an elliptical beam from the incoming beam with circular cross section. Both the turning prism and the telescope lenses have antireflection coatings for the second and third Nd:YAG harmonics, so that the measurements on both crystals can be compared without reflection loss adjustments. Both crystals have antireflection coatings for the two input wavelengths on their input facets but no coatings on their output facets.

FIGURE 5. Third stage of harmonic generator

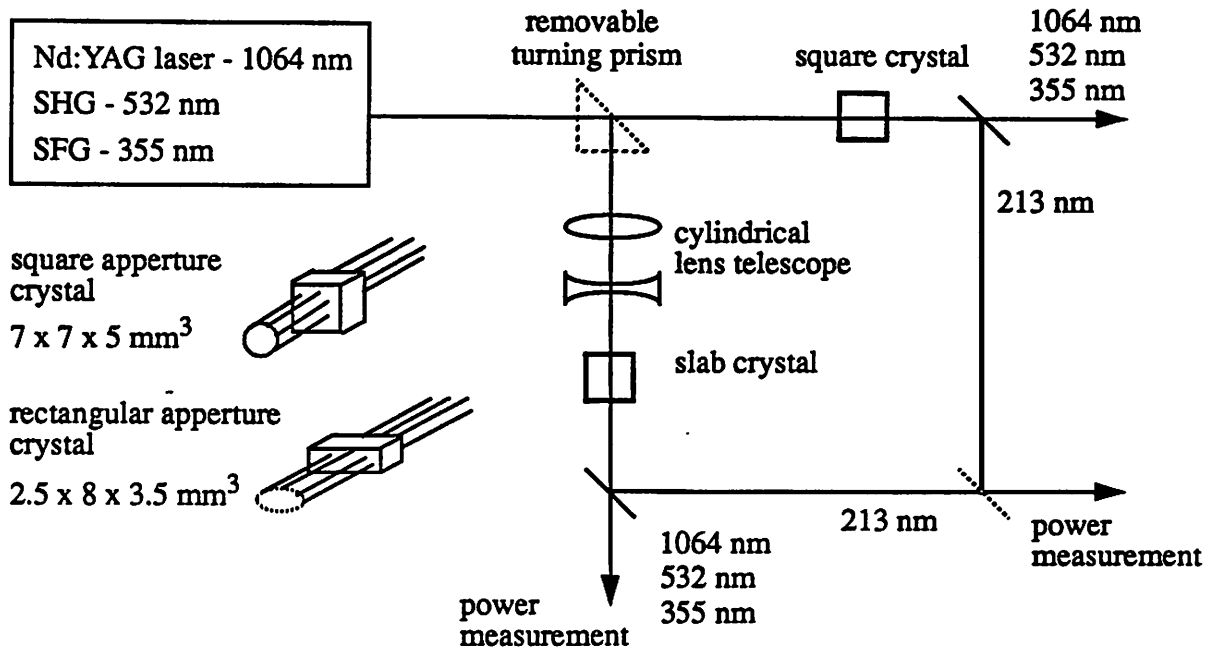

Control of the phase matching conditions for both crystals is provided by crystal ovens mounted on rotation stages, which enable angle tuning in the critical phase-matching direction. The square-aperture crystal is inside an aluminum heat sink without temperature control. The slab-shaped crystal is held in a temperature controlled oven at approximately 35 °C. The two long sides of the crystal are heat-sunk, while the two small sides are not. Thermal contact is provided by a thermally conductive elastomer sheet placed between the crystal and the oven.

In this conversion efficiency measurement, the generated 213-nm radiation was separated from the other harmonics with mirror filters oriented at 45° angle to the incident beams. Each mirror strongly reflects the 213-nm radiation (about 97%), while it transmits most of the power in the other harmonics (80-95 %). Before the fifth harmonic power was measured, the beam was reflected from several such mirrors so that no power at the other harmonics entered the detector. Similarly, the power in the other harmonics was determined by measuring the power in the beam transmitted by the 213-nm mirror. To separate the first, the second, and the third harmonics present in this beam, mirrors with high reflectivity at 1064 nm, 532 nm, and 355 nm were used. The mirror reflectivities needed for calculation of the power entering and exiting the crystal, were determined with the use of a spectrophotometer or by direct measurement. Comparison of the measured powers when the crystal generated the most power at 213 nm and when the crystal was detuned to produce no fifth-harmonic power was used to check the measured values, since it is known that 2/5 of the fifth harmonic power comes from the second harmonic and 3/5 comes from the third harmonic. The power was measured with two Scientech laser power meters, which absorb the laser light and determine the average laser power from the generated heat. The meter calibrated for detection of wavelengths in the 190-250 nm range was used to detect the

213-nm radiation. The other meter, calibrated for 400-1200 nm radiation, was used to detect the 1064-nm, 532-nm, and 355-nm light. Reflections at the detector surface were neglected in the calculations.

The measurements were performed under typical operating conditions of the system. The laser flashlamp power was relatively low to prevent crystal damage, which may occur when the system operates at maximum power. Consequently, the average output power at 213 nm was low in comparison to previous measurements [1]. The 213-nm average output power was in the 30-mW range when the square-shaped crystal was used as the third stage, and in the 70-mW range when the slab-shaped crystal was used. The measured conversion efficiency of both crystals was compared to calculated values. In the conversion efficiency calculations, material parameters in Table 1 and beam parameters in Table 5 were used. For the slab crystal, the beam size was adjusted by the compression factor of the lens telescope. In addition, beam quality factor Q of unity and uniform crystal temperature were used to determine the phase mismatch using Eq. (23). The calculations were done for both values of the effective nonlinear coupling d_{eff} in Table 1. Typical results are summarized in Table 13.

TABLE 13. Conversion efficiency of BBO I sum-frequency generator for producing 213 nm

		square crystal	slab crystal
213 nm average output power [mW]	P_5	32	74
355 nm average input power [mW]	P_3	192	192
532 nm average input power [mW]	P_2	221	221
measured efficiency	$\frac{P_5}{P_2+P_3}$	7.7 %	17.8 %
calculated efficiency (d_{eff} = 0.93 pm/V)		6.5 %	16.4 %
calculated efficiency (d_{eff} = 0.74 pm/V)		4.4 %	11.3 %

The calculated efficiencies are in good agreement with measurement results. Of the two values of the calculation parameter d_{eff}, the higher value predicts the measured efficiency within the measurement uncertainty. On the other hand, calculations with the lower d_{eff} value underestimate the measured conversion efficiency. Assuming that other calculation parameters represent the nonlinear interaction accurately, the nonlinear coupling strength of our BBO crystals seems to agree with the values obtained in [8].

6.2 Determination of crystal temperature

According to experimental evidence [1, 16] and to our calculations, crystal heating is expected to significantly influence the performance of the second generation 213-nm light source. Experimental verification of the predicted heating effects requires a method for measuring the crystal temperature during harmonic generation. Many standard thermometric techniques, such as the use of thermistors on the crystal surface or measurement of the changes in emitted blackbody radiation,

are not appropriate because bulk heating effects are important and resolution of several degrees Celsius at room temperature is needed. One possibly useful and relatively simple method for measuring the crystal temperature utilizes the pyroelectric effect. Pyroelectricity occurs in materials that lack inversion symmetry and consequently exists in the second-order nonlinear optical materials. The pyroelectric property results in a change in electric polarization when the crystal temperature is changed. A pyroelectric crystal with capacitor plates, formed by metal-coating the two facets normal to the direction of the dipole moment, will develop charge on its plates proportional to the temperature change [19]. The mean temperature change in the crystal can be measured using this effect. However, this effect has not yet been investigated in the materials under consideration here, so its sensitivity as a temperature indicator is questionable. Finally, the crystal temperature can be determined with optical interferometry. The most simple interferometric technique capable of providing information about the crystal temperature profile seems to be the following. A probe He-Ne laser beam is reflected from the crystal and the fringe pattern formed by interference of the two crystal facet reflections is observed [16]. The fringe pattern is a function of the optical path-length difference of the two reflected beams and depends on temperature. With the knowledge of the thermal expansion coefficients and of the refractive index change with temperature, temperature change can be calculated from changes in the fringe pattern.

The fringe method was tested in the third nonlinear stage of the first generation 213-nm system. The slab-shaped BBO crystal, cut for frequency up-conversion to 213 nm, was used in this measurement. Since only absorption at 213 nm is likely to be significant in BBO, negligible heating was expected at the current average power levels. Temperature sensitivity of the method was obtained by observation of the fringe pattern change with temperature and compared with that calculated from published data. The probe He-Ne beam entered the usual exit facet of the crystal, which had no anti-reflection coatings, at nearly normal incidence. The reflection off this facet interfering with the reflection from the usual input facet was recorded by a CCD camera. The fringe pattern was recorded at several crystal temperatures. First the crystal was heated with the oven to approximately 45 °C and then allowed to slowly cool to room temperature, while the readings were taken. Since the temperature was changing slowly, the crystal temperature was assumed to be the same as the oven temperature, determined from the resistance of the oven thermistor. The measurements were done when the probe beam was polarized both perpendicular and parallel to the plane of the optic axis and the beam. In the former case, the refractive index in the BBO crystal was the ordinary index, while in the latter case it was the extraordinary index at the angle of propagation with respect to the optic axis. Since the crystal is cut at angle $\theta = 69.5°$, this angle with $\pm 2°$ tolerance was used in the calculations. Thermal expansion data [5] were also needed to determine the optical path-length difference. In addition, the change in the refractive indices with temperature was assumed to be constant. The measurement results, as well as results expected from published data [5], are summarized in Table 14. The measurement temperature sensitivity, represented by the temperature change needed for a given position in the pattern to change from light to dark, equivalent to half-wavelength optical path-length change, is denoted by $\Delta T_{\lambda/2}$.

The temperature sensitivities calculated from published data are better than those actually observed. However, the crystal temperature change of several degrees Celsius can still be deter-

mined with this method. The discrepancy between the measurement and published data may be explained by the fact that the published values were comparable to the precision, with which they were determined [5]. Consequently, the change of refractive indices with temperature measured here should be closer to the actual values than the published data, provided that they are constant with temperature in the temperature range of this measurement.

TABLE 14. Temperature sensitivity of measurement

		published data	measurement
$\Delta T_{\lambda/2}$ *o*-ray	[°C]	4.2±0.9	11±1.8
e-ray		2.9±0.4	47±11
dn_o/dT	[10^{-5}/°C]	-1.66	-2.3±0.3
dn_e/dT		-0.93	-2.5±0.2

Once the measurement method was calibrated, the fringe pattern was observed during operation of the system. As expected at the operating power levels and the present measurement sensitivity levels, no change in the pattern was detected. However, this method may be useful for measuring the crystal temperature during harmonic conversion in the second generation 213-nm system.

7.0 Conclusion

The design of the optical frequency quintupler necessary to convert the 1064-nm Nd:YAG laser wavelength to the desired 213-nm wavelength has been considered in detail. At the high average power of the second generation system, thin-slab crystal geometry is superior to conventional crystal geometry with square input apertures. Slab geometry allows high efficiencies to be maintained even at relatively large average powers, because it improves heat extraction from the nonlinear crystals. This geometry requires an input beam with an elliptical cross section which can be produced by a series of four compressing prisms from the round-shaped Nd:YAG input beam. The best nonlinear optics design appears to be one that utilizes a BBO type I doubler as the first nonlinear stage. The choice for the second stage is a KD*P crystal oriented for type II phase matching that produces the third harmonic from its first and second harmonic inputs. The most efficient third stage, which adds the second and third harmonic frequencies to produce the fifth harmonic, is also a BBO crystal for type I mixing. Special waveplates are needed between the nonlinear stages to properly orient the output polarizations of each stage to the desired input polarizations of the following stage. This fifth harmonic generator would produce about 1 W of 213-nm radiation with 20-W input at 1064 nm.

Presently, BBO appears to be the most suitable nonlinear material for the multistage quintupler. However, LBO may prove to be more efficient than BBO in the 213-nm system, when it becomes more widely available and its thermal properties are determined. LBO is suitable fo- doubling and

tripling of Nd:YAG radiation and may prove useful for the first two stages of the system. One advantage of LBO over well developed materials like BBO and KD*P is its small walkoff angle and relatively short optimal crystal lengths. On the other hand, walkoff effects in BBO and KD*P are approximately the same. BBO has large walkoff angle but small optimum crystal lengths, while KD*P has somewhat smaller walkoff angles but requires longer crystal lengths. For both crystals, this leads to similar reduction in the spatial overlap of differently polarized beams.

The efficiency of the 213-nm system can be improved by correcting the walkoff effect. This is possible when two crystals are used for each nonlinear stage. For instance in uniaxial crystals, if one of the crystals is oriented at phase matching angle θ and the other is oriented at $-\theta$ or at $\pi - \theta$, the walkoff effect in the two crystals can cancel out, provided the crystal lengths are properly chosen. According to Appendix 1, the two differently oriented crystals may be chosen to have nonlinear coupling coefficient d_{eff} of same or opposite sign. If the two crystals are chosen to have nonlinear susceptibility of opposite sign and the length of the first crystal is $L = \pi/\Delta k$, the length at which the susceptibility changes sign and causes the generated beam to convert back to the input frequencies, the extraction of energy from the pump beams can continue in the second crystal [22]. Through this effect and reduction of the walkoff, greater efficiency is possible. Use of two crystals at each stage would improve the efficiency but also significantly increases the complexity of the system.

The performance of the system can also be enhanced by decreasing the beam and crystal size in order to increase intensities and improve heat extraction. Due to diffraction limitations, refocusing of the beam after each stage would be necessary to maintain small beam size. Refocusing could prove most effective before the third nonlinear stage, where the heating effects are most detrimental. Although this approach may be effective in improving efficiency, it may reduce the beam quality. In addition, the additional optical elements would increase the complexity and the cost of the system.

8.0 Acknowledgments

I would like to thank my advisor Professor W. G. Oldham for his help, guidance, and support in this project. I am grateful for having the opportunity to work in his group. I would also like to thank Professor J. Bokor for taking time to read this report. Finally, I would like to thank Anita K. Lee for helpful discussions of the Nd:YAG laser design portion of this project.

9.0 References

[1] W. N. Partlo, *Issues in Deep-UV Lithography Using Pulsed Laser Light Sources*, Ph. D. Thesis, University of California, Berkeley, Memorandum No. UCB/ERL M92/14, January 1992.

[2] A. K. Lee, in preparation, M. S. Project, University of California, Berkeley.

[3] L. Leinbaugh, *Design of a 5th Harmonic Generator for a Nd^{+}:YAG Laser Source for Optical Lithography*, M. S. Project, University of California, Berkeley, December 1992.

[4] D. Eimerl, "High average power harmonic generation", *IEEE Journal of Quantum Electronics*, **QE-23**, pp. 575-592, May 1987.

[5] D. Eimerl, L. Davis, S. Velsko, E. K. Graham, A. Zalkin, "Optical, mechanical, and thermal properties of barium borate", *Journal of Applied Physics*, **62**, pp. 1968-1983, 1987.

[6] C. Chen, B. Wu, A. Jiang, G. You, "A new type ultraviolet SHG crystal β-BaB_2O_4", *Scientia Sinica B*, **28**, pp. 235-243, 1985.

[7] C. Chen, Y. X. Fan, R. C. Eckardt, R. L. Byer, "Recent developments in barium borate", *Proceedings of the SPIE*, **681**, pp. 12-19, 1986.

[8] Y. X. Fan, R. C. Eckardt, R. L. Byer, C. Chen, A. D. Jiang, "Barium borate optical parametric oscillator", *IEEE Journal of Quantum Electronics*, **QE-25**, pp. 1196-1199, 1989.

[9] D. Eimerl, "Electro-optic, linear, and nonlinear optical properties of KDP and its isomorphs", *Ferroelectrics*, **72**, pp. 95-139, 1987.

[10] C. Chen, Y. Wu, A. D. Jiang, B. Wu, G. You, R. Li, S. Lin, "New nonlinear-optical crystal: LiB_3O_5", *Journal of the Optical Society of America B*, **6**, pp. 616-621, 1989.

[11] K. Kato, "Tunable UV Generation to 0.2325 μm in LiB_3O_5", *IEEE Journal of Quantum Electronics*, **QE-26**, pp. 1173-1175, 1990.

[12] S. P. Velsko, M. Webb, L. Davis, C. Huang, "Phase-matched harmonic generation in lithium triborate (LBO)", *IEEE Journal of Quantum Electronics*, **QE-27**, pp. 2182-2192, 1991.

[13] T. Ukachi, R. J. Lane, W. R. Bosenberg, C. L. Tang, "Measurements of noncritically phase-matched second-harmonic generation in a LiB_3O_5 crystal", *Applied Physics Letters*, **57**, pp. 980-982, 1990.

[14] A. Borsutzky, R. Brunger, R. Wallenstein, "Tunable UV radiation at short wavelengths (188-240 nm) generated by sum-frequency mixing in lithium borate", *Applied Physics B*, **52**, pp. 380-384, 1991.

[15] D. N. Nikogosyan, "Beta barium borate (BBO): A review of its properties and applications", *Applied Physics A*, **52**, pp. 359-368, 1991.

[16] S. C. Matthews, J. S. Sorce, "Fourth harmonic conversion of 1.06μ in BBO and KD*P", *Proceedings of the SPIE*, **1220**, pp. 137-147, 1990.

[17] C. A. Ebbers, J. Happe, N. Nielsen, S. P. Velsko, "Optical absorption at 1.06 μm in highly deuterated potassium dihydrogen phosphate", *Applied Optics*, **31**, pp. 1960-1964, 1992.

[18] H. S. Carslaw, J. C. Jaeger, *Conduction of Heat in Solids*, 2nd ed., Clarendon Press, Oxford, 1986.

[19] J. F. Nye, *Physical Properties of Crystals: Their Representation by Tensors and Matrices*, Clarendon Press, Oxford, 1985.

[20] Cleveland Crystals, unpublished observations.

[21] E. Kreyszig, *Advanced Engineering Mathematics*, 6th ed., John Wiley & Sons, 1988.

[22] J. A. Armstrong, N. Bloembergen, J. Ducuing, and P. S. Pershan, "Interactions between light waves in a nonlinear dielectric", *Physical Review*, **127**, pp. 1918-1938, September 15, 1962.

[23] M. Abramowitz and I. A. Stegun (eds.), *Handbook of Mathematical Functions* (9th printing), Dover Publications, New York, 1972.

[24] J. E. Midwinter, J. Warner, "The effects of phase matching method and of uniaxial crystal symmetry on the polar distribution of second-order non-linear optical polarization", *Brittish Journal of Applied Physics,* **16**, pp. 1135-1142, 1965.

[25] M. V. Hobden, "Phase-matched second-harmonic generation in biaxial crystals", *Journal of Applied Physics,* **38**, pp. 4365-4372, 1967.

A.0 Appendices

A.1 Effective nonlinear coupling

References [24, 25]

BBO:

type I (*oo-e*) $$d_{eff} = d_{15}\sin\theta - d_{22}\cos\theta\sin 3\phi \quad \text{(A1)}$$

type II (*eo-e*) $$d_{eff} = d_{22}\cos^2\theta\cos 3\phi \quad \text{(A2)}$$

KD*P:

type I (*oo-e*) $$d_{eff} = -d_{14}\sin\theta\sin 2\phi \quad \text{(A3)}$$

type II (*eo-e*) $$d_{eff} = d_{14}\sin 2\theta\cos 2\phi \quad \text{(A4)}$$

LBO type I (*pp-s*):

$$d_{eff} = d_{16}\cos^2\theta\sin\phi\sin 2\phi - \cos\phi\,((d_{21}\cos^2\phi + d_{22}\sin^2\phi)\cos^2\theta + d_{23}\sin^2\theta) \quad \text{(A5)}$$

θ=90°, *x-y* tuning $$d_{eff} = -d_{23}\cos\phi \quad \text{(A6)}$$

LBO type I (*ss-p*):

$$d_{eff} = d_{16}\cos\theta\cos\phi\sin 2\phi - \cos\theta\sin\phi\,(d_{21}\sin^2\phi + d_{22}\cos^2\phi) \quad \text{(A7)}$$

ϕ=0°, *x-z* tuning $$d_{eff} = 0 \quad \text{(A8)}$$

LBO type II (*sp-s*):

$$d_{eff} = d_{16}\cos\theta\sin\phi\cos 2\phi + \cos\theta\cos^2\phi\sin\phi\,(d_{21} - d_{22}) \quad \text{(A9)}$$

θ=90°, *x-y* tuning $$d_{eff} = 0 \quad \text{(A10)}$$

ϕ=90°, *y-z* tuning $$d_{eff} = -d_{16}\cos\theta \quad \text{(A11)}$$

A.2 Refractive indices

Uniaxial crystals:

$$\frac{1}{n_e(\theta)^2} = \frac{\cos^2\theta}{n_o^2} + \frac{\sin^2\theta}{n_e^2} \tag{A12}$$

Biaxial crystals:

$$\frac{1}{n_s(\phi)^2} = \frac{\sin^2\phi}{n_x^2} + \frac{\cos^2\phi}{n_y^2} \tag{A13}$$

$$\frac{1}{n_p(\theta,\phi)^2} = \cos^2\theta\left(\frac{\cos^2\phi}{n_x^2} + \frac{\sin^2\phi}{n_y^2}\right) + \frac{\sin^2\theta}{n_z^2} \tag{A14}$$

A.3 Dephasing parameters

$$\beta_\theta = \frac{2\pi}{\lambda}\left(a\frac{\partial n_{1\omega}}{\partial\theta} + b\frac{\partial n_{2\omega}}{\partial\theta} - c\frac{\partial n_{3\omega}}{\partial\theta}\right)\Bigg|_{\theta=\theta_m,\,\phi=\phi_m,\,T=T_0} \tag{A15}$$

$$\beta_\phi = \frac{2\pi}{\lambda}\left(a\frac{\partial n_{1\omega}}{\partial\phi} + b\frac{\partial n_{2\omega}}{\partial\phi} - c\frac{\partial n_{3\omega}}{\partial\phi}\right)\Bigg|_{\theta=\theta_m,\,\phi=\phi_m,\,T=T_0} \tag{A16}$$

$$\beta_T = \frac{2\pi}{\lambda}\left(a\frac{\partial n_{1\omega}}{\partial T} + b\frac{\partial n_{2\omega}}{\partial T} - c\frac{\partial n_{3\omega}}{\partial T}\right)\Bigg|_{\theta=\theta_m,\,\phi=\phi_m,\,T=T_0} \tag{A17}$$

A.4 MATLAB solution to heat equation

```
%%%   steady state temperature in the region -a<x<a, -b<x<b, -1/2<z<1/2 with
%%%   heat generation proportional to the incident intensity
%%%   nonzero thermal conductivity tensor elements: k11, k22, k33, k23=k32

%%%%%%%%%%%%%%%% thermal conductivities   %%%%%%%%%%%%%%%%%%%%%%%%%%%%%%%%
c11=k11;                                        % nonlinear crystal
c22=k11*cos(theta)^2+k33*sin(theta)^2;          % k11 and k22 defined elsewhere
c33=k11*sin(theta)^2+k33*cos(theta)^2;
d=(k33-k11)*sin(theta)*cos(theta);
h=0.0009;                                       % surface heat transfer W/cm2
to=0;                                           % air temperature
%%%%%%%%%%%%%%%%  grid   %%%%%%%%%%%%%%%%%%%%%%%%%%%%%%%%%%%%%%%%%%%%%%%%%
%% crystal dimensions (a, b, l), beam dimensions (wx, wy), and number of
%% grid points (pts) are defined elsewhere
xpt = pts;                  % number elements in x (excluding boundaries)
```

```
dx = 2*a/(xpt + 1);      % x spacing in cm
ypt = pts;               % number elements in y
y2=ypt+2;
dy = 2*b/(ypt + 1);      % y spacing in cm
zpt = pts;               % number elements in z
dz = 1/(zpt + 1);        % z spacing in cm
%%%%%%%%%%%%%%%  useful constants   %%%%%%%%%%%%%%%%%%%%%%%%%%%%%%%%%%%%
cx=c11/(dx^2);
cy=c22/(dy^2);
cz=c33/(dz^2);
dyz=d/(2*dy*dz);

xsample = floor((xpt+2)/2)+1;       % center point at these coordinates
ysample = floor((ypt+2)/2)+1;
zsample = floor((zpt+2)/2)+1;
[x,y] = meshdom(-a:dx:a,-b:dy:b);
%%%%%%%%%%  absorption   %%%%%%%%%%%%%%%%%%%%%%%%%%%%%%%%%%%%%%%%%%%%%%%%%
pin = 50;                           % incident power; W
plabs = 1;                          % absorbed power/length; W/cm

n=5;                                % exponent of supergaussians
integrate2d                         % find absorption profile normalization
areafactor=4*integral;              % effective beam area
c = plabs/areafactor;               % absorbed power/volume
[x,y] = meshdom(-a:dx:a,-b:dy:b);
absorb = c*exp(-2*((x/wx).^2+(y/wy).^2).^(n/2)).* ...  %% absorption profile
     (1-0.74*exp(-2*((1.5*x/wx).^2+(1.5*y/wy).^2).^(n/2)));

%%%%%%%%%%  temperature profile calculation  %%%%%%%%%%%%%%%%%%%%%%%%%%%%
[x,y,z] = meshgrid(1:1:xpt+2,1:1:ypt+2,1:1:zpt+2);
temp0=0*(x+y+z);                    % initialize temperature
rhs1=ones(xpt,1);                   % initialize vectors
rhs2=ones(ypt,1);
rhs3=ones(zpt,1);
x=1:xpt+2;
y=1:ypt+2;

temp=temp0;              % temperature in 3D crystal represented by 2D matrix
prevtemp=temp0;          % (dimension ((xpt+2)*(ypt+2)) x (zpt+2))
prevtemp0=temp0;

% tridiagonal matrices and their inverses
ma1 = diag(-2*(cx+cy+cz) .* ones(xpt,1)) ...
            +diag(cx*ones(xpt-1,1),1)+diag(cx*ones(xpt-1,1),-1);
ma2 = diag(-2*(cx+cy+cz) .* ones(ypt,1)) ...
            +diag(cy*ones(ypt-1,1),1)+diag(cy*ones(ypt-1,1),-1);
ma3 = diag(-2*(cx+cy+cz) .* ones(zpt,1)) ...
            +diag(cz*ones(zpt-1,1),1)+diag(cz*ones(zpt-1,1),-1);

inv1 = inv(ma1);
inv2 = inv(ma2);
inv3 = inv(ma3);

stop = 0;
```

```
z=0;
while stop == 0
  z=z+1;                                % iteration count

  for k=1:zpt,                          % solution along x direction
    for j=1:ypt,
      for n=1:xpt,
       rhs1(n) = -absorb(j+1,n+1) ...
                 -cy*(prevtemp(j+2+n*y2,k+1)+prevtemp(j+n*y2,k+1)) ...
                 -cz*(prevtemp(j+1+n*y2,k+2)+prevtemp(j+1+n*y2,k)) ...
                 -dyz*(prevtemp(j+2+n*y2,k+2)+prevtemp(j+n*y2,k) ...
                      -prevtemp(j+2+n*y2,k)-prevtemp(j+n*y2,k+2));
      end
      rhs1(1)=rhs1(1)-cx*prevtemp(j+1,k+1);
      rhs1(xpt)=rhs1(xpt)-cx*prevtemp(j+1+(xpt+1)*y2,k+1);
      newx=ones(xpt+2,1);
      newx(1,1) = temp(j+1,k+1); % constant T at endpoints
      newx(2:xpt+1,1) = inv1 * rhs1;              % newly computed
      newx(xpt+2,1) = temp(j+1+(xpt+1)*y2,k+1);
      temp(j+1+(x-1).*y2,k+1)=newx;
    end
  end
  % boundary condition at y=+-b
  temp(1+(x-1)*y2,2:zpt+1)=(h*to+c22/dy*temp(2+(x-1)*y2,2:zpt+1)+ ...
      d/(2*dz)*(temp(2+(x-1)*y2,3:zpt+2)-temp(2+(x-1)*y2,1:zpt)))/(h+c22/dy);
  temp(ypt+2+(x-1)*y2,2:zpt+1)= ...
       (h*to+c22/dy*temp(ypt+1+(x-1)*y2,2:zpt+1)- ...
        d/(2*dz)*(temp(ypt+1+(x-1)*y2,3:zpt+2)-...
                  temp(ypt+1+(x-1)*y2,1:zpt)))/ ...
       (h+c22/dy);
  % boundary condition at z=+-1/2
  for q=1:xpt+2,
   temp((2:ypt+1)+(q-1)*y2,1)=(h*to+c33/dz*temp((2:ypt+1)+(q-1)*y2,2)+ ...
        d/(2*dy)*(temp((3:ypt+2)+(q-1)*y2,2)-...
        temp((1:ypt)+(q-1)*y2,2)))/(h+c33/dz);
   temp((2:ypt+1)+(q-1)*y2,zpt+2)= ...
        (h*to+c33/dz*temp((2:ypt+1)+(q-1)*y2,zpt+1)- ...
        d/(2*dy)*(temp((3:ypt+2)+(q-1)*y2,zpt+1)-...
        temp((1:ypt)+(q-1)*y2,zpt+1)))/ ...
        (h+c33/dz);
  end

  % boundary conditions at edges y=+-b and z=+-1/2 (average)
  temp(1+(x-1)*y2,1)=0.5*((h*to+c22/dy*temp(2+(x-1)*y2,1)+ ...
         d/(2*dz)*(temp(2+(x-1)*y2,3)-temp(2+(x-1)*y2,1)))/(h+c22/dy))+...
                    0.5*((h*to+c33/dz*temp(1+(x-1)*y2,2)+ ...
         d/(2*dy)*(temp(3+(x-1)*y2,2)-temp(1+(x-1)*y2,2)))/(h+c33/dz));
  temp(ypt+2+(x-1)*y2,1)=0.5*((h*to+c22/dy*temp(ypt+1+(x-1)*y2,1)- ...
        d/(2*dz)*(temp(ypt+1+(x-1)*y2,3)-...
              temp(ypt+1+(x-1)*y2,1)))/(h+c22/dy))+...
                         0.5*((h*to+c33/dz*temp(ypt+2+(x-1)*y2,2)+ ...
        d/(2*dy)*(temp(ypt+2+(x-1)*y2,2)-...
              temp(ypt+(x-1)*y2,2)))/(h+c33/dz));
  temp(1+(x-1)*y2,zpt+2)=0.5*((h*to+c22/dy*temp(2+(x-1)*y2,zpt+2)+ ...
```

```
      d/(2*dz)*(temp(2+(x-1)*y2,zpt+2)-...
            temp(2+(x-1)*y2,zpt)))/(h+c22/dy))+...
                        0.5*((h*to+c33/dz*temp(1+(x-1)*y2,zpt+1)- ...
      d/(2*dy)*(temp(3+(x-1)*y2,zpt+1)-...
            temp(1+(x-1)*y2,zpt+1)))/(h+c33/dz));
temp(ypt+2+(x-1)*y2,zpt+2)=...
                  0.5*((h*to+c22/dy*temp(ypt+1+(x-1)*y2,zpt+2)- ...
      d/(2*dz)*(temp(ypt+1+(x-1)*y2,zpt+2)-...
            temp(ypt+1+(x-1)*y2,zpt)))/(h+c22/dy))+...
                  0.5*((h*to+c33/dz*temp(ypt+2+(x-1)*y2,zpt+1)- ...
      d/(2*dy)*(temp(ypt+2+(x-1)*y2,zpt+1)-...
            temp(ypt+(x-1)*y2,zpt+1)))/(h+c33/dz));

prevtemp0=prevtemp;
prevtemp=temp;

n=1:ypt;                              % solution along y direction
for i=1:xpt,
  for k=1:zpt,
    rhs2 = -absorb(n+1,i+1) ...
           -cx*(prevtemp(n+1+(i+1)*y2,k+1)+prevtemp(n+1+(i-1)*y2,k+1)) ...
           -cz*(prevtemp(n+1+i*y2,k+2)+prevtemp(n+1+i*y2,k)) ...
           -dyz*(prevtemp(n+2+i*y2,k+2)+prevtemp(n+i*y2,k) ...
              -prevtemp(n+2+i*y2,k)-prevtemp(n+i*y2,k+2));
    rhs2(1)=rhs2(1)-cy*prevtemp(1+i*y2,k+1);
    rhs2(ypt)=rhs2(ypt)-cy*prevtemp(ypt+2+i*y2,k+1);
    newy = ones(1,ypt+2);
    newy(1,1) = prevtemp(1+i*y2,k+1);
    newy(1,2:ypt+1) = (inv2 * rhs2)';
    newy(1,ypt+2) = prevtemp(ypt+2+i*y2,k+1);
    temp(y+i*y2,k+1)=newy';
  end
end
% boundary condition at y=+-b
temp(1+(x-1)*y2,2:zpt+1)=(h*to+c22/dy*temp(2+(x-1)*y2,2:zpt+1)+ ...
    d/(2*dz)*(temp(2+(x-1)*y2,3:zpt+2)-temp(2+(x-1)*y2,1:zpt)))/(h+c22/dy);
temp(ypt+2+(x-1)*y2,2:zpt+1)= ...
     (h*to+c22/dy*temp(ypt+1+(x-1)*y2,2:zpt+1)- ...
      d/(2*dz)*(temp(ypt+1+(x-1)*y2,3:zpt+2)-...
                temp(ypt+1+(x-1)*y2,1:zpt)))/ ...
     (h+c22/dy);
% boundary condition at z=+-1/2
for q=1:xpt+2,
 temp((2:ypt+1)+(q-1)*y2,1)=(h*to+c33/dz*temp((2:ypt+1)+(q-1)*y2,2)+ ...
      d/(2*dy)*(temp((3:ypt+2)+(q-1)*y2,2)-...
      temp((1:ypt)+(q-1)*y2,2)))/(h+c33/dz);
 temp((2:ypt+1)+(q-1)*y2,zpt+2)= ...
      (h*to+c33/dz*temp((2:ypt+1)+(q-1)*y2,zpt+1)- ...
      d/(2*dy)*(temp((3:ypt+2)+(q-1)*y2,zpt+1)-...
      temp((1:ypt)+(q-1)*y2,zpt+1)))/ ...
      (h+c33/dz);
end
% boundary conditions at edges y=+-b and z=+-1/2 (average)
temp(1+(x-1)*y2,1)=0.5*((h*to+c22/dy*temp(2+(x-1)*y2,1)+ ...
```

```
        d/(2*dz)*(temp(2+(x-1)*y2,3)-temp(2+(x-1)*y2,1)))/(h+c22/dy))+...
                  0.5*((h*to+c33/dz*temp(1+(x-1)*y2,2)+ ...
        d/(2*dy)*(temp(3+(x-1)*y2,2)-temp(1+(x-1)*y2,2)))/(h+c33/dz));
temp(ypt+2+(x-1)*y2,1)=0.5*((h*to+c22/dy*temp(ypt+1+(x-1)*y2,1)- ...
      d/(2*dz)*(temp(ypt+1+(x-1)*y2,3)-...
            temp(ypt+1+(x-1)*y2,1)))/(h+c22/dy))+...
                  0.5*((h*to+c33/dz*temp(ypt+2+(x-1)*y2,2)+ ...
      d/(2*dy)*(temp(ypt+2+(x-1)*y2,2)-...
            temp(ypt+(x-1)*y2,2)))/(h+c33/dz));
temp(1+(x-1)*y2,zpt+2)=0.5*((h*to+c22/dy*temp(2+(x-1)*y2,zpt+2)+ ...
      d/(2*dz)*(temp(2+(x-1)*y2,zpt+2)-...
            temp(2+(x-1)*y2,zpt)))/(h+c22/dy))+...
                  0.5*((h*to+c33/dz*temp(1+(x-1)*y2,zpt+1)- ...
      d/(2*dy)*(temp(3+(x-1)*y2,zpt+1)-...
         - temp(1+(x-1)*y2,zpt+1)))/(h+c33/dz));
temp(ypt+2+(x-1)*y2,zpt+2)=...
                  0.5*((h*to+c22/dy*temp(ypt+1+(x-1)*y2,zpt+2)- ...
      d/(2*dz)*(temp(ypt+1+(x-1)*y2,zpt+2)-...
            temp(ypt+1+(x-1)*y2,zpt)))/(h+c22/dy))+...
                  0.5*((h*to+c33/dz*temp(ypt+2+(x-1)*y2,zpt+1)- ...
      d/(2*dy)*(temp(ypt+2+(x-1)*y2,zpt+1)-...
            temp(ypt+(x-1)*y2,zpt+1)))/(h+c33/dz));

prevtemp=temp;

n=1:zpt;                              % solution along z direction
for i=1:xpt,
  for j=1:ypt,
    rhs3 = (-1)*absorb(j+1,i+1)*ones(1,zpt) ...
           -cx*(prevtemp(j+1+(i+1)*y2,n+1)+prevtemp(j+1+(i-1)*y2,n+1)) ...
           -cy*(prevtemp(j+2+i*y2,n+1)+prevtemp(j+i*y2,n+1)) ...
           -dyz*(prevtemp(j+2+i*y2,n+2)+prevtemp(j+i*y2,n) ...
           -prevtemp(j+2+i*y2,n)-prevtemp(j+i*y2,n+2));
    rhs3(1)=rhs3(1)-cz*prevtemp(j+1+i*y2,1);
    rhs3(zpt)=rhs3(zpt)-cz*prevtemp(j+1+i*y2,zpt+2);
    newz = ones(1,zpt+2);
    newz(1,1) = prevtemp(j+1+i*y2,1);
    newz(1,2:zpt+1) = (inv3 * rhs3')';
    newz(1,zpt+2) = prevtemp(j+1+i*y2,zpt+2);
    temp(j+1+i*y2,:)=newz;
  end
end
% boundary condition at y=+-b
temp(1+(x-1)*y2,2:zpt+1)=(h*to+c22/dy*temp(2+(x-1)*y2,2:zpt+1)+ ...
    d/(2*dz)*(temp(2+(x-1)*y2,3:zpt+2)-temp(2+(x-1)*y2,1:zpt)))/(h+c22/dy);
temp(ypt+2+(x-1)*y2,2:zpt+1)= ...
     (h*to+c22/dy*temp(ypt+1+(x-1)*y2,2:zpt+1)- ...
      d/(2*dz)*(temp(ypt+1+(x-1)*y2,3:zpt+2)-...
                temp(ypt+1+(x-1)*y2,1:zpt)))/ ...
     (h+c22/dy);
% boundary condition at z=+-1/2
for q=1:xpt+2,
 temp((2:ypt+1)+(q-1)*y2,1)=(h*to+c33/dz*temp((2:ypt+1)+(q-1)*y2,2)+ ...
      d/(2*dy)*(temp((^:ypt+2)+(q-1)*y2,2)-...
```

```
        temp((1:ypt)+(q-1)*y2,2)))/(h+c33/dz);
    temp((2:ypt+1)+(q-1)*y2,zpt+2)= ...
        (h*to+c33/dz*temp((2:ypt+1)+(q-1)*y2,zpt+1)- ...
        d/(2*dy)*(temp((3:ypt+2)+(q-1)*y2,zpt+1)-...
        temp((1:ypt)+(q-1)*y2,zpt+1)))/ ...
        (h+c33/dz);
  end
  % boundary conditions at edges y=+-b and z=+-1/2 (average)
  temp(1+(x-1)*y2,1)=0.5*((h*to+c22/dy*temp(2+(x-1)*y2,1)+ ...
        d/(2*dz)*(temp(2+(x-1)*y2,3)-temp(2+(x-1)*y2,1)))/(h+c22/dy))+...
                0.5*((h*to+c33/dz*temp(1+(x-1)*y2,2)+ ...
        d/(2*dy)*(temp(3+(x-1)*y2,2)-temp(1+(x-1)*y2,2)))/(h+c33/dz));
  temp(ypt+2+(x-1)*y2,1)=0.5*((h*to+c22/dy*temp(ypt+1+(x-1)*y2,1)- ...
        d/(2*dz)*(temp(ypt+1+(x-1)*y2,3)-...
              temp(ypt+1+(x-1)*y2,1)))/(h+c22/dy))+...
                        0.5*((h*to+c33/dz*temp(ypt+2+(x-1)*y2,2)+ ...
        d/(2*dy)*(temp(ypt+2+(x-1)*y2,2)-...
              temp(ypt+(x-1)*y2,2)))/(h+c33/dz));
  temp(1+(x-1)*y2,zpt+2)=0.5*((h*to+c22/dy*temp(2+(x-1)*y2,zpt+2)+ ...
        d/(2*dz)*(temp(2+(x-1)*y2,zpt+2)-...
              temp(2+(x-1)*y2,zpt)))/(h+c22/dy))+...
                        0.5*((h*to+c33/dz*temp(1+(x-1)*y2,zpt+1)- ...
        d/(2*dy)*(temp(3+(x-1)*y2,zpt+1)-...
              temp(1+(x-1)*y2,zpt+1)))/(h+c33/dz));
  temp(ypt+2+(x-1)*y2,zpt+2)=...
                0.5*((h*to+c22/dy*temp(ypt+1+(x-1)*y2,zpt+2)- ...
        d/(2*dz)*(temp(ypt+1+(x-1)*y2,zpt+2)-...
              temp(ypt+1+(x-1)*y2,zpt)))/(h+c22/dy))+...
                        0.5*((h*to+c33/dz*temp(ypt+2+(x-1)*y2,zpt+1)- ...
        d/(2*dy)*(temp(ypt+2+(x-1)*y2,zpt+1)-...
              temp(ypt+(x-1)*y2,zpt+1)))/(h+c33/dz));

  prevtemp=temp;
  % relative error between successive iterations
  test = (temp(ysample+(xsample-1)*y2,zsample)- ...
          prevtemp0(ysample+(xsample-1)*y2,zsample)) / ...
          temp(ysample+(xsample-1)*y2,zsample);
  if (test >0 & test <= 0.005) | (test<0 & test >= -0.005),
    stop = 1;
  end
end

% temperature at crystal cross sections
xyplane=zeros(xpt+2,ypt+2);                    % xy plane sample
for q=1:xpt+2,
 xyplane(q,:)=temp(y+(q-1)*y2,zsample)';
end
yzplane=temp(y+(xsample-1)*y2,:);              % yz plane sample
xzplane=temp(ysample+(x-1)*y2,:);              % xz plane sample
tmax=max(max(temp));                           % maximum temperature
```